Reduced Order Model for Simultaneous Growth of Multiple Closely-Spaced Radial Hydraulic Fractures

C. Cheng[1], A. P. Bunger[2,1,*]

[1]Department of Chemical and Petroleum Engineering, University of Pittsburgh, Pittsburgh, PA, USA

[2]Department of Civil and Environmental Engineering, University of Pittsburgh, Pittsburgh, PA, USA

[*]Corresponding Author: bunger@pitt.edu

Abstract

A new reduced order model (ROM) provides rapid and reasonably accurate prediction of the complex behavior of multiple, simultaneously growing radial hydraulic fractures. The method entails vastly reducing the degrees of freedom typically associated with fully-coupled simulations of this multiple moving boundary problem by coupling together an approximation of the influence of the stress interaction among the fractures ("stress shadow") with an approximation of fluid flow and elasticity, ensuring preservation of global volume balance, global energy balance, elasticity, and compatibility of the crack opening with the inlet fluid flux. Validating with large scale ("high-fidelity") simulations shows the ROM solution captures not only the basic suppression of interior hydraulic fractures in a uniformly-spaced array due to the well-known stress shadowing phenomenon, but also complex behaviors arising when the spacing among the hydraulic fractures is non-uniform. The simulator's usefulness is

demonstrated through a proof-of-concept optimization whereby non-uniform spacing and stage length are chosen to maximize the fracture surface area and/or the uniformity of growth associated with each stimulation treatment.

KEYWORDS: Hydraulic fracturing; Reduced order model; Optimization; Multiple fracture growth

1 Introduction

Reduced order models (ROMs) have a great potential for enabling optimization and uncertainty quantification for hydraulic fracturing. However, ascertaining the essential ingredients necessary for a reasonably accurate and suitable efficient ROM for simulating systems of multiple, simultaneously-growing hydraulic fractures remains a challenging and open problem.

Hydraulic fracturing (HF) is a well stimulation technique used in many industrial applications include mining, waste disposal, and enhanced geothermal systems [1-3] The most well-known application is its use for increasing the rate at which oil and gas can be extracted from wells. In this application, pressurized fluid drives growth of cracks through the reservoir rock, carrying granular proppant that is left behind in the created fractures. The resulting high conductivity pathways promote an increased flow of hydrocarbons from the reservoir formation towards the well (as described in further detail by e.g.[4]). Both vertical and horizontal wells are stimulated in this way, with vertical well simulation comprising most cases over the 70 year history of hydraulic fracturing and horizontal well fracturing comprising the essential advance for unlocking unconventional (low-permeability) resources in the past two to three decades [5]. Essentially all horizontal wells in unconventional reservoirs (such as shale gas and oil) are treated by hydraulic fracturing, and the most common approach is to stimulate in a sequential manner from the "toe" to the "heel" of the well (see description in e.g.[6]). Within each of these sequential "stages", multiple clusters of perforations comprise the reservoir entry points, with the intention that injected fluid is reasonably uniformly distributed among these possible entry points, thereby uniformly stimulating the reservoir rock. Although such a multistage technique has enabled tremendous cost savings, analysis of production logs over several basins tends to show that between 20 to 40 percent of perforation clusters do not contribute to production [7], indicating current simulation strategies are highly non-optimal. One contributing factor is the non-uniformity of reservoir properties, including the in-situ stresses along the well e.g.[8,9]. Another factor is almost certainly the widely recognized phenomenon known of "stress shadowing" (see e.g. field evidence in [10]). Stress shadowing refers to suppression of some HFs as a result of the compressive stresses exerted on them by other, nearby HFs (e.g.[11-13]). One result is that the ideal case of uniform hydraulic fracture growth (Fig. 1a) is probably never achieved. Instead, some hydraulic fractures are suppressed due to the presence of locally elevated compressive stress (Fig. 1b as previously discussed by e.g.[14], see also. [11,12,15,16,17,18]).

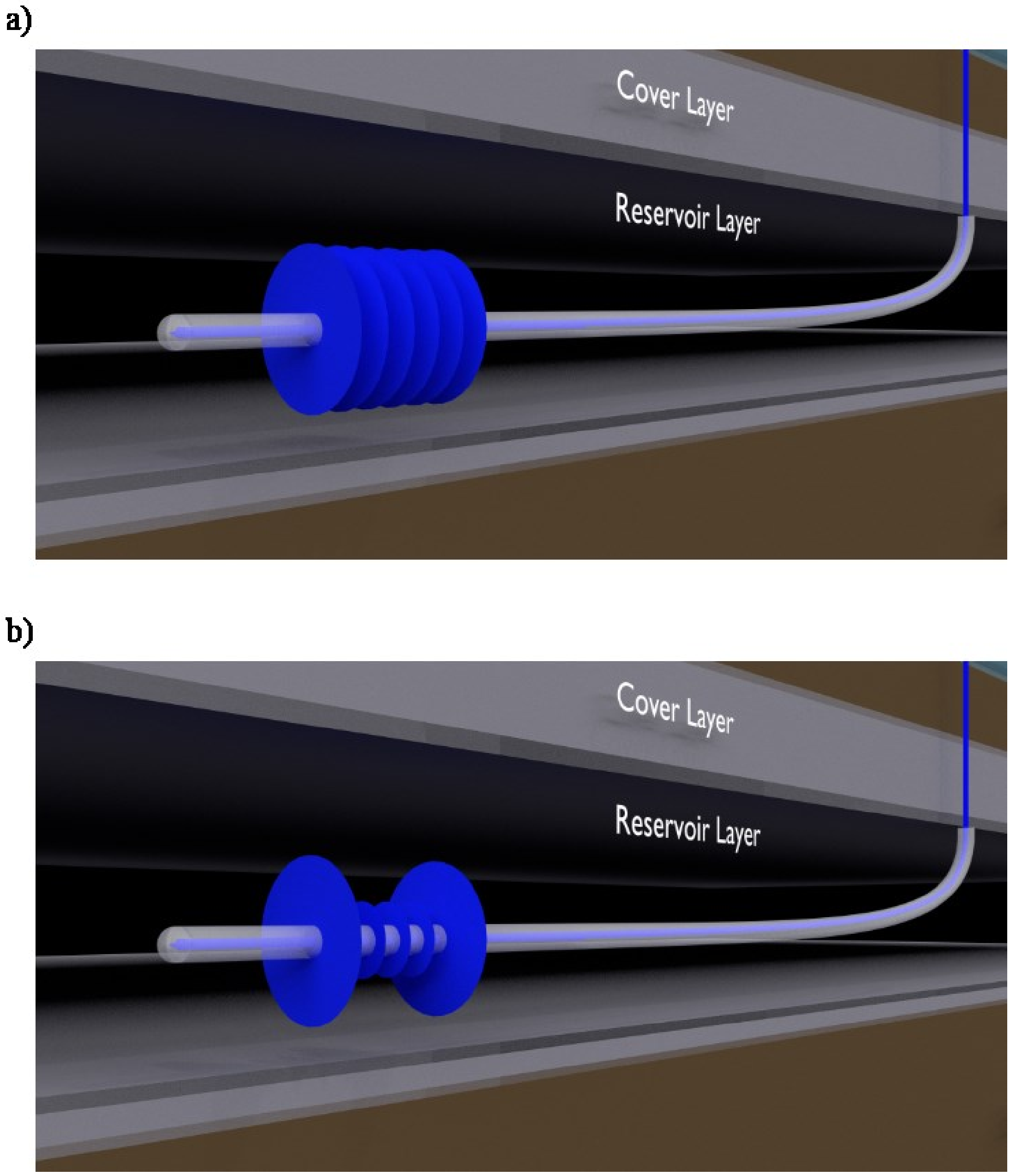

Fig. 1. Illustration of multiple, simultaneous HFs in one stage showing. (a) Ideal, uniform result, and (b) Result in which central fractures are suppressed.

While there are certainly demonstrations showing use of hydraulic fracture simulators to identify approaches that improve uniformity of stimulation (see e.g.[6,19]), optimization is challenging because of the simulations' computational intensity. Overcoming this challenge has opened a growing area of interest in generating reduced order models for hydraulic fractures, for example following formalisms that involve order reduction via an empirical search for eigenfunction bases that can be used to capture system behavior over some subdivision of the time domain ([20-24]). Here we follow a different approach, but the goal is the same, namely, to obtain a reduced order model that provides a useful approximation to the full model, and with the key feature being capturing interaction of simultaneously growing hydraulic fractures.

While there are several possible threads in the literature that aim generally at simulating and optimizing multistage completions, here we will briefly introduce the background most relevant to the current contribution. The Implicit Level Set Algorithm, or “ILSA” [25] was extended by [19] for multiple parallel-planar HFs, including full 3D elastic coupling between the simultaneously propagating fractures (“ILSA II”). This simulator has been used to demonstrate that the stress shadow effect can be reduced with appropriate placement of interior HFs close to the outer HFs to inhibit their growth relative to the other fractures in the array.

Although ILSA II is a fully coupled benchmark simulator (to use terminology commonly contrasted with ROMs, we also can call this a “large scale” or “high-fidelity” model), implementing state of the art approaches to enable accurate calculations on very coarse meshes, the model can require several days, and sometimes over one week, to compute a multi-fracture result at typical reservoir length and time scales (note timing is for single node calculations, ~2.5 GHz processor speed). Hence, optimization of HF design, which can require hundreds or thousands of model runs, is not practical with this or other models with run times on the order of tens of hours to days. Similarly, uncertain quantification, which also can require thousands or model evaluations, is not typically possible. A first step is, therefore, addressing the need for rapid, even if approximate, simulation. Such ROM simulators can be used to do broad explorations of high dimensional parametric spaces, identifying combinations of parameters, which can be examined in detail by a few, fully-coupled simulations.

We previously demonstrated the feasibility and basic concept of a new HF simulator, called "C2Frac", which very rapidly estimates the growth of an array of HFs [26]. In this prototype model, the HFs are restricted to radial, planar growth - as in the current version presented here - but under the additional limitation that fractures remain small in radius compared to their separation. The method uses semi-analytical HF solutions (after [27]), coupling a far field approximation of the interaction stress via an overall energy balance. In this way, the model predicts each HF's aperture $W_i(t)$, net pressure $P_i(t)$, radius $R_i(t)$, and inflow rate $Q_i(t)$ for different choices of uniform or non-uniform spacing among N HFs. The validating shows good agreement between C2Frac and ILSA II benchmarks, however, because of the use of a far-field approximation of the interaction stress between the HFs, the C2Frac estimates diverge from fully coupled benchmark solutions when the fracture radii become similar to the fracture spacing. Additionally, because the prototype model does not account for near field stress interaction, it does not capture some of the complex behaviors predicted by fully coupled simulations when the fracture spacing is non-uniform. In particular, the previous model cannot capture when the interior fractures switch from being suppressed to accepting the majority of the fluid, as observed in fully-coupled simulations by [19]. Simulating this phase is essential for obtaining accurate predictions, but it can only be captured when the impacts of near field stress interaction between very closely spaced fractures are appropriately modeled.

The necessary model improvements are here enabled by developing a new algorithm leading to numerical simulations approximating the benchmark solutions for all times, regardless of fracture radius and spacing, while running 10^3-10^6 times faster than the fully coupled benchmark simulator. In this paper, the new model, called "C3Frac", is developed and validated. We begin by presenting the governing equations. We then introduce a new approach to approximation of the interaction stress from each fracture based on a uniformly pressurized crack with equal volume and radius to the actual HF. Next, we describe an interaction stress coupled elasticity function, which preserves volume balance by ensuring the elasticity solution is consistent with the inlet flow rate boundary condition. Then, the system of governing equations is completed by requiring that the fluid is partitioned among the multiple entry points so as to maintain equality of the wellbore pressure predicted for each fracture while also conserving the fluid injected into the wellbore. These final conditions are required by both the fully coupled and approximate simulator. In the case of the fully coupled simulator the wellbore pressure is predicted by carefully simulating fluid flow at all locations within the fracture so as to obtain an accurate estimate of the pressure at the fracture inlet (wellbore). In contrast, the approximate simulator approximates the fluid flow in a manner preserving the main contribution to viscous energy dissipation and then predicts the inlet pressure for each fracture using global energy balance.

After presenting the model, we next show how well it approximates the fully coupled simulations. Following this validating, numerical experiments illustrate cases for uniform and non-uniform spacing designs to indicate how spacing effects the hydraulic fracture growth. Thus, we utilize the new C3Frac model to search for optimized HF scenarios in terms of created fracture surface area, providing examples of optimized designs for different stage lengths, inflow rates, and pumping times. The work concludes with a demonstration of the benefits of optimization and the potential for non-uniform fracture spacing to promote multiple methods for promoting multiple HF growth.

2 Governing Equations

In a typical HF treatment of an oil or gas well, one or more fractures is/are created by injection of fluid. The fracture is initiated within a rock formation that contains the hydrocarbons (the reservoir), and propagates perpendicularly to the orientation of the minimum in situ confining stress σ_o. Here the HFs are considered to grow transversely to a horizontal well, as illustrated by Fig. 1. This model accounts for the growth of N fractures within a single stage and, for now, neglects the stresses induced by the previous stages [28-30], noting that these can be important especially if they induce substantial fracture curving. Furthermore, we note that if the fracture curving is negligible (see [31] for one approach for ascertaining if the curving will be important), then these previous-stage stresses can be accounted for with a straightforward extension of the approach wherein the stresses from fractures in the previous stage(s) are accounted for in the same manner as we account for fracture induced stresses within the same stage. The model, then, considers an array of N planar fractures distributed within one stage of length Z (see Fig. 2). Hence, the spacing h_k, k=1,..N-1 between each of the fractures is such that:

$$Z = \sum_{k=1}^{N-1} h_k \tag{1}$$

Growth of the array of HFs is driven by injection of an incompressible fluid from a wellbore at the center of each of the radially-growing HFs (Fig. 1). The rate provided to each HF is variable and determined as a part of the solution, however, to conserve fluid in the wellbore, the influx rates to each fracture must always sum to a constant total volumetric rate Q_o. This is to say that we consider the total fluid injection rate provided to the wellbore to be a constant, but the partitioning of this fluid to each fracture to be transient. The HFs are taken to propagate quasi-statically (i.e. well below the speed of sound for the rock) in a permeable, linear elastic rock characterized by $E' = E/(1-\nu^2)$ for Young's modulus E, Poisson's ratio ν, and toughness $K' = (32/\pi)^{1/2} K_{IC}$ for fracture toughness K_{IC} (after [27]). Solution to the problem consists of determining the partitioning of the influx to each HF as well as each HF's crack width, net pressure, and radius. Several additional assumptions are introduced to simplify this problem:

(I) Crack propagation follows linear elastic fracture mechanics (LEFM), which assumes that the material follows a linear elastic stress-strain relationship everywhere except for in a very small "process zone" near the crack tip [32]. Crack propagation will occur when the opening-mode stress intensity at the crack tip attains the material fracture toughness [33,34].

(II) Lubrication theory is used to describe laminar flow of a Newtonian fluid within the fracture (e.g.[35]).

(III) The rock is impermeable, and hence the leak off term is not considered in this study (i.e. it is not considered in the fluid mass balance of Eq. (2)).

(IV) All HFs grow radially and parallel to one another.

(V) Gravitational force is neglected both in the elasticity and fluid flow equations.

(VI) The fluid front is coincident with the crack front, meaning the lag between the fluid front and fracture tip is very small compared to the fracture radius, which is valid under typical high confinement conditions encountered in reservoirs [31].

(VII) The far field in situ stress σ_o is uniform and constant, although the total compressive stress acting on each fracture is, of course, non-uniform and non-constant due to the interaction with its neighbors.

For a detailed discussion of several of these common assumptions in hydraulic fracture modeling, especially regimes of small versus large viscosity and small versus large leakoff, see Detournay [48]. We also idealize that, for the entire period of growth, the fractures remain planar and radial, as illustrated by Fig. 2. Again we note that this idealization neglects deviation of the fracture path either due to interaction with natural fractures or due to stress shadowing from other HFs [16,30,31,37,38,39,40]. It also neglects the presence of a height growth barrier which is present in most reservoirs and leads to a transition from radial to blade-like growth (called the "PKN" geometry after [41,42]). Based on similar arguments to those described in detail by [19], this model is expected to remain valid for gently curving HFs, as long as the impact of the curving on the energy required to drive the HFs represents a small correction to the leading order term(s) used by this model. However, it is also clearly possible that the stress interaction will be affected by the curving and, in the context of a coupled model where small perturbations can sometimes be amplified, it is possible that scenarios in which the curving significantly impacts behavior will be discovered as a part of future research. Furthermore, ongoing efforts will aim at capturing the transition to PKN-like growth, but the present model is limited to the radial growth period that persists as long as the fracture radius does not exceed the lithologically-limited fracture height. An additional, important limitation in scope is that here the near-wellbore pressure losses due to fracture tortuosity and/or perforation friction and pressure loss associated with fluid flow through the inside of the casing between the perforation clusters are neglected. These, too, are readily accounted for, through incorporated into the power balance as one power contribution to preserve the inlet pressure condition [43,44], but not the focus of this paper. Finally, accounting for interaction with natural factures is a challenge which remains for future research and is not addressed here.

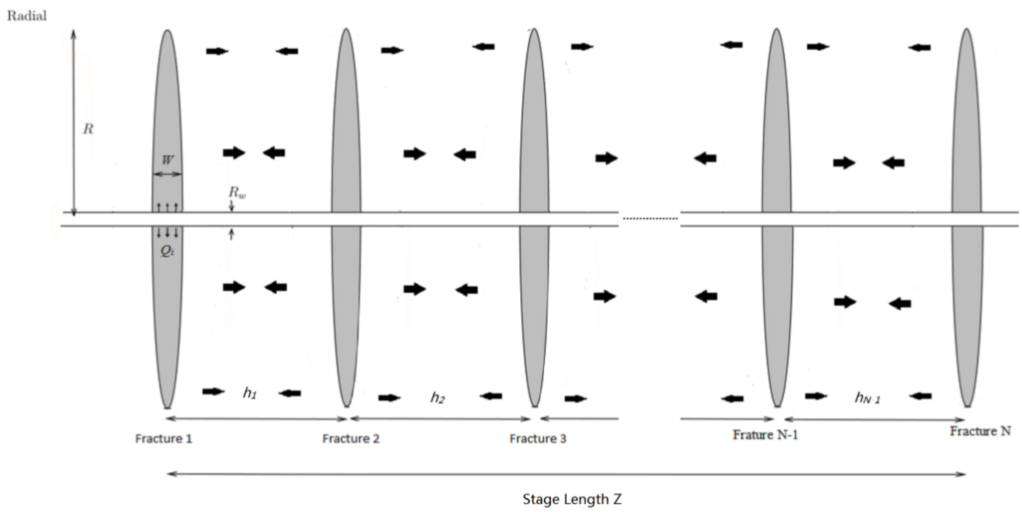

Fig. 2. Geometry of the multiple HF problem for N HFs distributed within a stage of

length Z and with fracture spacing h_k . The arrows illustrate the interaction stresses between fractures.

Having established the simplifying assumption, we return to the description of the model itself. For an array of N fractures, there are $5N$ unknowns. They are, for the i^{th} fracture, the opening $w_i(r,t)$, fluid pressure $p_{f(i)}(r,t)$, fracture radius $R_i(t)$, elastic interaction stress from the other fractures $\sigma_{I(i)}(r,t)$, and inlet flow rate $Q_i(t)$, where $i=1,\ldots,N$ (see Fig. 2). These quantities are governed by a manifestation of a classical HF model bringing together elastic deformation of the HF, fluid mass balance, laminar fluid flow, and an LEFM crack propagation criterion [45], with an addition of an elastic expression of the interaction stress (after [46]) and a condition of pressure and fluid continuity within the wellbore (after e.g.[19]). Specifically, the model begins firstly with fluid continuity (mass balance) which, based on the assumptions of an incompressible fluid and an impermeable rock, is given for the i^{th} fracture by

$$\frac{\partial w_i(r,t)}{\partial t}+\frac{1}{r}\frac{\partial r q_i(r,t)}{\partial r}=0 \tag{2}$$

where q is the flow rate across the fracture aperture (width), that is, $q=\langle v\rangle w$ for mean velocity $\langle v\rangle$.

Secondly, the elastic body is considered to be deformed by a traction T_i acting across the surfaces of each fracture. In the case of interacting circular cracks, the elasticity relationship between local normal traction T and width w is given by [46]

$$w_i(r,t)=\frac{8R_i(t)}{\pi E'}\mathcal{F}\{\rho_i,T_i(\rho_i,t)\} \qquad \rho_i=r/R_i(t) \tag{3}$$

Here the non-local integral operator $\mathcal{F}$ and internal traction acting on each fracture T_i are given in Section 3.

Thirdly, according to lubrication theory for an incompressible Newtonian fluid [47], the radial flux $q_i(r,t)$ is proportional to the gradient of the fluid pressure via the classical Poiseuille law, that is

$$q_i(t) = -\frac{w_i(r,t)^3}{12\mu}\frac{\partial p_{f(i)}(r,t)}{\partial r} \tag{4}$$

where μ is the dynamic viscosity. Fourthly, according to Assumption (I) (linear elastic fracture), the crack always propagates in limit equilibrium, and hence the fracture propagation criterion takes the form

$$K_I = K_{Ic} \tag{5}$$

where K_I denotes the mode I (opening) stress intensity factor and K_{Ic} the model I fracture toughness. For the radial fracture, K_I can be expressed as [32]

$$K_I = 2\sqrt{\frac{R_i(t)}{\pi}}\int_0^1 \frac{T_i(\rho_i,t)}{\sqrt{1-{\rho_i}^2}}\rho_i d\rho_i \tag{6}$$

Fifthly, injection of fluid from the borehole is imposed at the center of each fracture. Hence, based on mass balance considerations, the boundary condition at the inlet of the crack is given by the source condition for each fracture

$$2\pi \lim_{r\to R_w} r q_i(r,t) = Q_i(t) \tag{7}$$

where R_w is the radius of the wellbore.

Sixthly, the boundary conditions at the crack tip are given by zero opening and zero flux $w_i(R_i,t)=0$, $q_i(R_i,t)=0$ [48,49] the initial condition ($t=0$) is given by $R_i=0$, $w_i=0$, and $p_{f(i)}=0$.

Note that with these initial and boundary conditions, the fluid continuity Eq. (2)

can be integrated to give a global mass balance equation which, although it does not provide an additional independent equation (it follows directly from equations already defined), is useful for simulation. This equation is given by

$$\int_0^t Q_i(t)dt = 2\pi \int_0^{R_i(t)} w_i(r,t) r dr \tag{8}$$

Also, by substitution of the Poiseuille Eq. (4) into the continuity Eq. (2), we obtain the Reynold's lubrication equation given by

$$\frac{\partial w_i(r,t)}{\partial r} = \frac{1}{12\mu}\frac{1}{r}\frac{\partial}{\partial r}\left(r w_i(r,t)^3 \frac{\partial p_{f(i)}(r,t)}{\partial r}\right) \tag{9}$$

Recall that 5N equations are required to solve for the 5N unknown quantities: fracture opening $w_i(r, t)$, fluid pressure $p_{f(i)}(r, t)$, radius $R_i(t)$, elastic interaction stress from the other fractures $\sigma_{I(i)}(r, t)$, and inlet flow rate $Q_i(t)$. So far we have defined 3N equations which are provided by the coupled system of partial-integro-differential equations from Reynolds lubrication equation for laminar fluid flow (Eq. (9)), elasticity (Eq. (3)), and propagation (Eq. (5)). An additional *N* equations are obtained from the interaction stresses which occur when multiple hydraulic fractures grow in close proximity to one another. An approximation of these stresses is described in Section 3.1. Hence, the system is closed firstly by the *N*-1 equations given by the constraint that the pressure is the same at every entry point (because they are tied by the wellbore)

$$p_{f(1)}(R_w,t) = p_{f(2)}(R_w,t) = \cdots = p_{f(N)}(R_w,t) \tag{10}$$

Note that a perforation friction loss term can be included [43,44], leaving Eq. (10) intact but providing a pressure loss between the wellbore pressure and the fluid pressure at the first point within the hydraulic fracture. The system is closed, then, with one equation from the constraint that the sum of fluid injected to all entry points must equal the total injection rate Q_o, that is

$$\sum_{i=1}^{N} Q_i(t) = Q_o \tag{11}$$

These form a complete system for determining $w_i(r;\, t)$, $p_{f(i)}(r;t)$, $R_i(t)$, $\sigma_{I(i)}(r;t)$, and $Q_i(t)$. The problem, then, consists of finding these unknowns as a function of given quantities Q_o, μ', K', E', R_w, N, h_k, and t, where $\mu'=12\,\mu$, for dynamic viscosity μ, all other quantities are as previously defined, starting from known values of these quantities at an initial time t_0.

3 Approximation

3.1 Interaction Stress Approximation

The main challenge and interest of the problem is due to HF interaction. In general, the interaction stresses need to be computed based on the details of the pressure distribution inside each HF (as in e.g. [19]). However, such an approach is not compatible with the desire for rapid, approximate computation. So, for this model, we propose an approximation of the interaction stress using the uniformly-pressurized crack solution of [50], whereby the normal component of stress performed by neighboring crack j on crack i is determined as

$$\sigma_{j.i} = \frac{2P_j}{\pi}\left\{\delta_{j,i}{}^{-\frac{1}{2}} cos\frac{1}{2}\varphi_{j,i} - tan^{-1}\frac{\delta_{j,i}{}^{\frac{1}{2}} sin\frac{1}{2}\varphi_{j,i} + \tau_{j,i} sin\theta_{j,i}}{\delta_{j,i}{}^{\frac{1}{2}} cos\frac{1}{2}\varphi_{j,i} + \tau_{j,i} cos\theta_{j,i}} \right.$$
$$\left. + \zeta_{j,i}\delta_{j,i}{}^{-\frac{3}{2}} cos\left(\frac{3}{2}\varphi_{j,i} - \theta_{j,i}\right) - \zeta_{j,i}\delta_{j,i}{}^{-\frac{1}{2}} sin\frac{1}{2}\varphi_{j,i}\right\} \tag{12}$$

where

$$\tau_{j,i} = \left(1+\zeta_{j,i}^2\right)^{\frac{1}{2}} \qquad \delta_{j,i} = \left\{\left[\left(\rho_i \frac{R_i}{R_j}\right)^2 + \zeta_{j,i}^2 - 1\right]^2 + 4\zeta_{j,i}^2\right\}^{\frac{1}{2}}$$

$$\theta_{j,i} = arctan\left(\frac{1}{\zeta_{j,i}}\right) \qquad \varphi_{j,i} = arccot\left\{\left[\left(\rho_i \frac{R_i}{R_j}\right)^2 + \zeta_{j,i}^2 - 1\right]/2\zeta_{j,i}\right\} \tag{13}$$

Recall that $\zeta_{j,i}$ is the ratio of spacing $h_{j,i}$ (between fracture *i* and *j*) to the crack radius R_j, and recalling that ρ_i is the ratio of radial position *r* to fracture radius R_i, $\rho_i = \frac{r}{R_i}$. Note that the $\zeta_{j,i}$ value decreases as the fracture grows, that is, as R_i increases for each fracture.

In the solution presented in Eq. (12), P_j is a uniform internal net pressure. The key to the approximation, then, is to choose this internal pressure so as to best approximate the actual interaction stress produced by HFs with non-uniform internal pressure. The approach used here is to select this uniform pressure for each HF at each time step so as to generate a fracture with the same volume as the actual HF being opened by a non-uniform internal pressure. That is, for the j^{th} hydraulic fracture the classical expression for the volume of an ellipsoidal crack resulting from uniform internal pressurization [50] leads directly to

$$P_j = \frac{3}{16}\frac{E'V_j}{{R_j}^3} \qquad V_j = \int_0^t Q_j dt \tag{14}$$

The interaction stress model is completed by summation of the interaction stress for each fracture from all neighbors. Hence the interaction stresses exerted on the i^{th} hydraulic fracture is approximated as

$$\sigma_{I(i)} = \sum_{i=1}^{N,j\neq i} \sigma_{j,i}\left[\rho_i R_i/R_{j,}\zeta_{j,i,}V_j, t, P_j\right] \tag{15}$$

where $\sigma_{j,i}$ is given by Eq. (12) and P_j is given by Eq. (14).

3.2 Approximating Elasticity and Fluid Flow

Elasticity, crack propagation, and fluid flow are strongly coupled through Eq. (3). The non-local integral operator $\mathcal{F}$ and internal traction acting on each fracture are given by

$$\mathcal{F}\{\rho_i, T_i(\rho_i, t)\} = \int_{\rho_i}^{1} \frac{s}{\sqrt{s^2-\rho_i^2}} \int_0^1 \frac{x T_i(xs,t)}{\sqrt{1-x^2}} dx ds$$
$$T_i(\rho_i, t) = p_{f(i)}(\rho_i R_i, t) - \sigma_{I(i)}(\rho_i R_i, t) - \sigma_o \tag{16}$$

recalling that where the σ_o is the far field stress, and $\sigma_{I(i)}$ is the interaction stress defined by Eq. (15). Additionally, $\zeta_{j,i}$ is the ratio of spacing $h_{j,i}$ (between fracture *i* and *j*) to the crack radius R_j (see Section 3.1), and $p_{f(i)}(r,t)$ is the fluid pressure, a part of the solution. In general, a complete solution is required simultaneously satisfying all of the relevant governing equations. But, the computational intensity of such a solution is the reason why fully coupled models require large computational times. To promote rapid computation, we will approximate this solution. Here we begin by expressing the fluid pressure as

$$p_{f(i)}(r,t) = \left(\frac{\mu' E'^2}{t}\right)^{\frac{1}{3}} \Pi_i(\rho_i, t) + \sigma_o, \qquad \rho_i = r/R_i(t)$$
$$\Pi_i(\rho_i, t) \cong A_i(t)\left[\omega - \frac{2}{3(1-\rho_i)^{\frac{1}{3}}}\right] - B\left(ln\frac{\rho_i}{2} + 1\right), \qquad \omega \approx 2.479 \tag{17}$$

This form of the pressure is taken based on the solution of [27] for a viscosity dominated, radially-growing hydraulic fracture in an impermeable rock. When considering the self-similar solution for zero toughness and constant injection rate for an HF propagating in an infinite, homogeneous elastic rock, [27] shows that $A_i(t) = 0.3581$ and $B = 0.09269$. While this solution only applies for this self-similar limit, we borrow its form for our approximation because it preserves the well-known behavior of the pressure at the tip and inlet of a propagating HF [51], which ought to also be present for interacting hydraulic fractures with non-constant influx rates, that is

$$\begin{aligned} p_{f(i)} &\sim \frac{2}{3}\left(1-\rho_i\right)^{-\frac{1}{3}}, 1-\rho_i \ll 1 \\ p_{f(i)} &\sim -\ln \rho_i , \rho_i \ll 1 \end{aligned} \tag{18}$$

The overall premise is that a solution of this form ought to be reasonably compatible with the consequences of coupling between elasticity and fluid flow in the limit where the energy dissipation associated with fluid flow is far greater than the energy dissipation associated with rock breakage (viscosity-dominated regime, see [52] for a more complete discussion). It remains to choose the coefficients, and we find that a usefully accurate approximation can be obtained (as shown in Section 4) by setting $B=0.09269$ and solving for the values of the $A_i(t)$ coefficients that preserve global volume balance for each fracture (Eq. (8)). Hence, $A_i(t)$ is a time dependent variable chosen to satisfy

$$2\pi\gamma_i(t)^2 L_i(t)^2 W_i(t) \int_0^1 \Omega_i(\rho_i, A_i(t))\rho d\rho - \int_0^t Q_i(t)dt = 0 \tag{19}$$

where the characteristic width

$$W_i(t) = \left(\frac{Q_i(t)\mu'}{2\pi B\left(\frac{\mu' E'^2}{t}\right)^{1/3}}\right)^{1/3} \tag{20}$$

represents the near well-bore width derived from Poiseuille law by extracting the leading order behavior of Eq. (4) at inlet to relate the fluid flux to the fluid pressure gradient, where $p_{f(i)} \sim B\ln(r)$ for $r \ll R_i$. Here B is the inlet asymptotic coefficient given by [27]. Note that the dominance of this term near the inlet and the equality of the inlet pressures (Eq. 11) justify setting B equal for all HFs. Similarly, drawing again on the viscosity regime scaling from [27], the radius is given by

$$R_i(t) = \gamma_i(t)\left(\left(\frac{E't}{\mu'}\right)^{1/3}\int_0^t Q_i(t)dt\right)^{1/3} \tag{21}$$

where $\gamma_i(t)$ are unknown values of dimensionless radius for each HF. These are obtained through a requirement that the opening at the HF centers obtained from elasticity, accounting for interaction stress, is compatible for each HF with the width obtained from Eq. (20). To do this, substitution of Eq. (17) in Eq. (3) introduces a dimensionless crack opening $\Omega_i(\rho_i, A_i(t))$ which is determined by $w_i(\rho_i, A_i(t))/\ w_i(0, A_i(t))$ as

$$\Omega_i(\rho_i, A_i(t)) = \mathcal{F}\{\rho_i, T_i(\rho_i, A_i(t))\}/\mathcal{F}\{0, T_i(\rho_i, A_i(t))\} \tag{22}$$

with $\mathcal{F}$ denoting the non-local integral as Eq. (3) shown and $T_i(\rho, A_i(t), t)$ is the traction acting across the surfaces of the i^{th} crack given by

$$\begin{aligned} T_i(\rho_i, A_i(t), t) = \left(\frac{\mu' E'^2}{t}\right)^{\frac{1}{3}} \Bigg\{ A_i(t)\left[\omega - \frac{2}{3(1-\rho_i)^{\frac{1}{3}}}\right] \\ - B\left(ln\frac{\rho_i}{2} + 1\right)\Bigg\} - \sum_{j=1}^{N, j\neq i} \sigma_{j,i}\left[\rho_i \cdot \frac{R_i(t)}{R_j(t)}, \zeta_{j,i}, t\right] \end{aligned} \tag{23}$$

where again we recall that $\sigma_{j,i}$ denotes the interaction stress performed by the neighboring fractures j loading on fracture i (see Section 3.1). The coefficient $A_i(t)$ is still unknown. The strategy, then, is to choose this correspondence between the pressure and opening via Eqs. (3) and (17), and in this way we ensure compatibility of the solution with elasticity, as shown by Eq. (24).

We arrive to a system of *2N* equations for the unknown quantities $\gamma_i(t)$ and $A_i(t)$ that impose: 1) satisfying global volume balance for each HF, and 2) requiring the HF opening at the center, computed from elasticity and including the interaction stress, to be compatible with the opening required by Eq. (20). Hence

$$\left\{\begin{array}{c} 2\pi\gamma_i(t)^2 L_i(t)^2 W_i(t)\int_0^1 \Omega_i\big(\rho_i, A_i(t)\big)\rho_i d\rho_i = \int_0^t Q_i(t)dt \\ \dfrac{4\gamma_i(t)L_i(t)}{\pi E'}\mathcal{F}\{0, T_i(\rho_i, A_i(t), t)\} = W_i(t) \end{array}\right\} \xrightarrow{yields} \left\{\begin{array}{c}\gamma_i(t)\\ A_i(t)\end{array}\right\} \tag{24}$$

3.3 Motivation for Energy Calculation

It is useful at this point to summarize. The model presented here is constructed so that it first and foremost exactly satisfies global fluid volume balance for each fracture. The solution is also constructed so that the correspondence between the fluid pressure and HF opening exactly satisfies elasticity equation for each fracture, up to a scaling of the elasticity equation by the HF radius, which is chosen via γ_i to ensure that the elastically-determined width at the inlet is compatible with the influx boundary condition. Hence, we have replaced the need to solve for 3N unknowns (w_i, p_i, R_i) based on 3N equations given by elasticity, propagation, and lubrication (Eqs. (3), (6), and (9), respectively) with 2N unknowns (γ_i and A_i) satisfying 2N equations given by Eq. (24). These, of course, depend implicitly upon the calculation of the interaction stress, which we recall proceeds from Eq. (15) using the solution for a uniformly pressurized crack with the same volume as the actual HF.

Besides approximating the interaction stress, the present solution method replaces the propagation conditions K_I=K_{IC} for each HF with a zero-toughness tip asymptote compatible with elasticity and fluid flow and which is implicit in the form of the pressure and opening solutions chosen here (see detailed discussions in [27,48,52]). Hence, the solution henceforth is applicable to only the viscosity-dominated regime of hydraulic fracture propagation. Generalization to finite toughness HFs is a subject of ongoing work.

Importantly, for the present solution method, we must realize that Reynold's lubrication equation is rather harshly approximated by simply ensuring global volume balance and a functional form of the pressure and opening expected to arise at the inlet and tip of the HF. Furthermore, the pressure gradient implied by the lubrication equation is very large near the inlet (Eq. (18)). Between these issues, it becomes unreliable to use the distribution of the pressure from Eq. (17) to compute the inlet pressures for the purpose of imposing the equal inlet pressure boundary condition (Eq. (10)). We therefore adopt an alternative where the inlet pressure for each HF is computed in order to satisfy a global energy balance. These energetically-computed pressures are then set equal to one another, providing an additional N-1 equations satisfying pressure continuity along the wellbore (Eq. 10), noting that at this point additional energy loss due to perforations is readily accounted for (after [43]). When combined with the condition that the sum of the influxes equal a constant total wellbore pumping rate (Eq. (11)), we obtain in total an additional N equations by which we determine the N unknown values of the fracture influxes, $Q_i(t)$.

3.4 Balancing Input Power

The expression for the input power is obtained by equating the hydraulic rate of work (product of the pressure and inflow rate) to terms associated with various energy storage, work, and dissipation terms, that is (after [53,54])

$$p_{f(i)}(R_w,t)Q_i(t) = \dot{U_\iota} - \dot{W_{o(\iota)}} - \dot{W_{I(\iota)}} + D_{c(i)} + D_{f(i)} \tag{25}$$

where:

- U is a portion that goes into increasing the strain energy by deforming the rock strain energy – this is the recoverable elastic energy.
- W_o is the work done on the crack by the in-situ stress – the hydraulic input power must be sufficient to overcome this negative work.
- W_I is the work done on each HF by the compressive stresses induced by its neighbors – again the hydraulic input power must be sufficient to overcome this negative work.
- D_c is the dissipation rate associated with rock breakage.
- D_f is the dissipation rate associated with viscous fluid flow.

Note that, consistent with the present limitation to the viscosity regime, without further loss of generality we can assume $D_c \ll D_f$, and hence D_c is neglected. The remaining terms can be defined following from basic continuum mechanics definitions. Here we make use of the form already derived by [26] whereby

$$\dot{U_\iota} = \pi \int_{R_w}^{R_i} \left(T_i \frac{\partial w_i}{\partial t} + w_i \frac{\partial T_i}{\partial t} \right) r dr \tag{26}$$

$$\dot{W_{o(\iota)}} = -Q_i \sigma_o \tag{27}$$

$$\dot{W_{I(\iota)}} = -2\pi \left(\int_{R_w}^{\min(R_i, R_j)} \sigma_{I(i)} \frac{\partial w_j}{\partial t} r dr + \sigma_{I(i)} \frac{dR_i}{dt} R_i w_j (\frac{R_i}{R_j}) \right) \tag{28}$$

$$D_{f(i)} = \frac{\pi}{\mu'} \int_{R_w}^{R_i} {w_i}^3 \left(\frac{\partial p_{f(i)}}{\partial r} \right)^2 r dr \tag{29}$$

Upon substitution unknowns A_i and γ_i with explicit dependence upon the unknown Q_i via the expression for W_o and with implicit dependence on Q_i via the solutions pressure, width, and radius expressions. Additionally, in order to rapidly estimate the time derivatives, they are approximated over a single time step according to the power law growth of width, length, and pressure given by the single fracture solution of Savitski and Detournay [27]. As such, the dimensionless width, length and pressure rate is set to be consistent with power law growth of 1/9, 4/9 and 1/3 powers, respectively. Bringing all of this together we obtain

$$\dot{U_\iota} = \sum_{j=1}^{N, j\neq i} \pi \gamma_i(t)^2 \left(-\frac{2}{9}\right) \left(\frac{\mu' E'^2 \langle Q_i(t) \rangle^3}{t} \right)^{\frac{1}{3}} \int_0^1 \Omega_i(\rho_i, A_i(t)) \Pi_{net(i)}(\rho_i, A_i(t)) \rho d\rho \tag{30}$$

$$\dot{W_{I(\iota)}} = -\sum_{j=1}^{N, j\neq i} \left\{ \begin{array}{c} \pi min\{R_i, R_j\} \\ \int_0^{min\left\{\frac{R_i}{R_j}, 1\right\}} \sigma_{I(i)} \left(\rho_i \frac{R_i}{R_{j,}} t \right) \frac{dw_j}{dt} \rho_j d\rho_j \\ +2\pi \left(\frac{\langle Q_j(t) \rangle \mu'}{2\pi B \left(\frac{\mu' E'^2}{t} \right)^{1/3}} \right)^{1/3} R_i \frac{dR_i}{dt} \sigma_{I(i)}(1, t) \Omega_j \left(\frac{R_i}{R_j}, A_j(t) \right) \end{array} \right\} \tag{31}$$

$$\dot{D_{f,p(\iota)}} = \pi \left(\frac{\langle Q_i(t) \rangle^3 E'^2 \mu'}{2\pi B t} \right)^{\frac{1}{3}} \int_0^1 \Omega_i \left(\rho_i, A_i(t) \right)^3 \left[\left(\frac{\partial \Pi_{f(i)}(\rho_i, A_i(t))}{\partial \rho_i} \right)^2 - \left(\frac{B}{\rho_i} \right)^2 \right] \rho_i d\rho_i \tag{32}$$

$$\dot{D_{f,\ln(\iota)}} = \pi \left(\frac{\langle Q_i(t) \rangle^3 E'^2 \mu'}{2\pi B t} \right)^{\frac{1}{3}} \int_0^1 \Omega_i(0, A_i(t))^3 \left(\frac{B}{\rho_i} \right)^2 \rho_i d\rho_i \tag{33}$$

where R is given by Eq. (21).

3.5 Summary and Implementation

The final version of the minimalist simulator satisfies:

- Volume balance globally.
- Poiseuille flow via an approximation that preserves the appropriate behavior of the pressure near the tip and inlet, i.e. where most of the viscous dissipation takes place.
- The interaction stress based on the solution for a uniformly pressurized crack with the same radius and volume.
- The width-pressure elasticity relationship exactly.
- Propagation exactly, here limiting consideration to vanishingly small fracture toughness.
- The condition of equal inlet pressures exactly, with the wellbore approximated for each HF so as to be compatible with each HF's global energy balance.
- The condition that the fracture influxes sum to the total injection rate exactly.

Such an approach allows an ROM entailing solution of $3N$ equations for 3N unknowns, with simple functional relationships connecting all other quantities. In contrast, to solve the original problem using a fully meshed simulator, even a boundary element-type (BEM) simulator, would require solving for $2N$ unknowns corresponding the HF lengths and influxes plus an additional $4NM^2$ for the nodal values of the pressure, width, flux, and interaction stress on an MxM mesh for each HF in the array. If the mesh consists of 10-1000 elements in each direction, the ROM represents a reduction in degrees of freedom on the order of 10^1-10^6 compared to a large-scale model. Indeed this will be shown to be on the order of the factor by which the computational times differ between the ROM and benchmark simulations. The algorithm used by C3Frac to implement this approach is as follows:

1) User inputs: Set values for the physical parameters $\{E, v, K_{IC}, \mu, Q, Z, \sigma_{min}, R_w, h_{i,j}\}$ as well as the initial time, final time, and time step for the calculation, $\{t_0; t_f; \Delta t\}$, respectively.

2) Pre-guessed state: Set $Q_i^{(k);1} = Q_i^{(k-1)}$. Then fluid pressure $p_{f(i)}^{(k);1}$, length $R_i^{(k);1}$, width $w_i^{(k);1}$ of each HF (i = 1,…, N) is predicated according to Eq. (17), (20) and (21).

$$w_i^{(k);1}(\rho) = \left(\frac{\mu'^2\left[Q_i(t^{(k)})^{(k);1}\right]^3 t^{(k)}}{E'^2}\right)^{1/9} \Omega_i(\rho_{i'}, A_i(t)^{(k);1})^{(k);1}$$

$$R_i^{(k);1} = \left(\left(\frac{E' t^{(k)}}{\mu'}\right)^{\frac{1}{3}} Q_i(t^{(k)})^{(k);1} t^{(k)}\right)^{\frac{1}{3}} \gamma_i^{(k);1}$$

$$P_i^{(k);1}(\rho) = \left(\frac{\mu' E'^2}{t^{(k)}}\right)^{1/3} \Pi_{net(i)}\big(\rho_i, A_i(t)\big)^{(k);1}$$

For the first-time step, the dimensionless parameters for a viscosity-dominated HF are presented by [27] with small adjustments to the coefficients demonstrated by [26]. The interaction stress is estimated as Eq. (15):

$$\sigma_{I(i)}^{(k);1} = \sum_{j=1}^{N, j\neq i} \sigma_{j,i}^{(k);1}\left[\rho_i \gamma_i^{(k)} R_i^{(k);1}/R_j^{(k);1}, \frac{h_{j,i}}{R_j^{(k);1}}\right]$$

3) Then the $A_i^{(k);1}$ and $\gamma_i^{(k);1}$ are solved by the system Eq. (24):

$$\begin{cases} 2\pi\left(\gamma_i^{(k);1} L_i\left(t^{(k)}\right)^{(k);1}\right)^2 W_i\left(t^{(k)}\right)^{(k);1} \int_0^1 \Omega_i(\rho_i, A_i(t)^{(k);1})^{(k);1} \rho_i d\rho_i \\ \quad - \int_0^{t^{(k)}} Q_i\left(t^{(k)}\right)^{(k);1} dt = 0\,, \qquad i = 1, \dots, N \\ \dfrac{4\gamma_i^{(k);1} L_i\left(t^{(k)}\right)^{(k);1}}{\pi E'} \mathcal{F}\left\{0, T_i(\rho_i, A_i(t)^{(k);1}, t^{(k)})\right\} \\ \quad - W_i\left(t^{(k)}\right)^{(k);1} = 0, \qquad i = 1, \dots, N \end{cases}$$

4) To obtain the solution, the system of equations is solved numerically using Newton's method. Based on the above calculated value, the stress strain coupled local crack opening, net pressure and radius is numerically evaluated. We then substitute the stress coupled $\Omega_i^{(k);1}$,$\gamma_i^{(k);1}$ into the power balance function. Use non-linear solver (e.g. Matlab "fsolve") to obtain the N influxes $Q_i^{(k);2}$ simultaneously satisfying the constraints that the pressure at the inlet of all of the fractures is the same (i.e. connected by a horizontal wellbore with negligible friction loss along the wellbore between the entry points) and a further constraint that the sum of all influxes to the fractures must equal the total influx to the well. That is,

$$p_{f(1)}{}^{(k)}(R_w) = p_{f(2)}{}^{(k)}(R_w) = \cdots = p_{f(N)}{}^{(k)}(R_w), \qquad \sum_{i=1}^{N} Q_i{}^{(k)} = Q_o$$

Here a critical point is that the pressures are estimated using the energy balance equation via Eq. (25). Upon substitution of the estimates for the power terms Eqs. (20), (21) and (30)-(33) this estimate is

$$
\begin{aligned}
&p_{f(i)}^{(k);n}(R_w) = \sigma_o + \ldots \\
&\frac{1}{Q_i^{(k);n}}\left[\begin{array}{l}
-\dfrac{2}{9}\left(\dfrac{E'^2\left(Q_i^{(k);n}\right)^3\mu'}{t^{(k)}}\right)^{1/3}\displaystyle\int_0^1 \Pi_{net(i)}{}^{(k);n}\Omega_i{}^{(k);n}\rho_i d\rho_i - \ldots \\
2\pi\left\{\begin{array}{l}
\left(\dfrac{1}{9}\right)\displaystyle\sum_{j=1}^{N,j\neq i}\left\{\begin{array}{l}
\dfrac{w_j^{(k);n}}{t^{(k)}}\left[\min\left(R_i^{(k);n},R_j^{(k);n}\right)\right]^2 * \ldots\ldots \\
\displaystyle\int_0^{\min\left(R_i^{(k);n}/R_j^{(k);n},1\right)}\sigma_I\left(\rho_i\dfrac{R_i^{(k);n}}{R_j^{(k);n}},\zeta_{j,i}^{(k);n}\right)\Omega_j^{(k);n}\rho_j d\rho_j
\end{array}\right\} + \ldots \\
\left(\dfrac{4}{9}\right)\dfrac{\left(R_i^{(k);n}\right)^2}{t^{(k)}}\displaystyle\sum_{j=1}^{N,j\neq i} w_j^{(k);n}\Omega_j^{(k);n}\left(R_i^{(k);n}/R_j^{(k);n}\right)\sigma_I\left(1,\zeta_{j,i}^{(k);n}\right)
\end{array}\right\} + \ldots \\
0.04637\left(\dfrac{E'^2\mu'\left(Q_i^{(k);n}\right)^3}{t^{(k)}}\right)^{1/3}\ln\left(\dfrac{R_w^9\mu'}{E'\left(Q_i^{(k);n}\right)^3\left(t^{(k)}\right)^4}\right)^{1/9} + \ldots \\
\left(\dfrac{E'^2\mu'\left(Q_i^{(k);n}\right)^3}{t^{(k)}}\right)^{1/3}\displaystyle\int_0^1\left(\Omega_i^{(k);n}\right)^3\left(\left(\dfrac{\partial\Pi_{f(i)}{}^{(k);n}}{\partial\rho_i}\right)^2 - \dfrac{B^2}{\rho_i{}^2}\right)\rho_i d\rho_i
\end{array}\right]
\end{aligned}
$$

Note the simplicity of the modification, illustrating the potential to include other mechanisms (e.g. fluid leakoff, perforation loss and previous stage effect) in a straightforward manner provided their contribution to the global energy balance can be computed.

5) Check the relative difference between initially guessed $Q_i^{(k);1}$ and returned $Q_i^{(k);2}$. If the value is below a given tolerance that is

$$\left[Q_i^{(k);N} - Q_i^{(k);N-1}\right]/Q_i^{(k);N-1} < TOL$$

then output the $Q_i^{(k);2}$ as the final result. If not, iterate to convergence.

6) Repeat steps (2)-(5) until $t^{(k)} = t$.

Note that the new C3Frac bears a few similarities to the previously-published C2Frac [26]. Similarities include they both solve the flow rate based on the power balance with Newtonian numerical method. However, the striking and important difference lies in the solution of width, radius and pressure, which is solved by using an asymptotic solution [after 27] in C2Frac. In contrast, C3Frac uses Eq. (24) to obtain the non-self-similar solution caused by the inconstant flow rate with interaction stress included. The result is that C3Frac and C2Frac give very similar predictions when the fracture radii are less than the fracture spacing, and they diverge as the fractures continue their growth such that the courser approximation of the interaction stress and elasticity equation used in C2Frac becomes less accurate.

4 Validating and Overall Behavior of the Solution

We validate and illustrate the use of the model considering cases with 5 HFs. The fractures are placed symmetrically relative to the middle fracture. Hence the "outer" fractures, 1 and 5, are identical. So also the "inner" fractures, 2 and 4, are identical. Fracture 3 always occupies the center of the array and will henceforth be called the "middle" fracture. The validating is comprised of comparison of the C3Frac approximations (ROM) to fully coupled large-scale ("high fidelity") simulations obtained using ILSA II (after [19], using similar validating cases to [26]). ILSA II is extended for multiple, parallel planar hydraulic fractures [19] based on the Implicit Level Set Algorithm ("ILSA") [25] ILSA by accounting for full 3D elastic coupling between the simultaneously propagating fractures. The Implicit Level Set Algorithm ("ILSA") is a fully coupled simulator for 3D hydraulic fractures under the constraint that fracture growth is confined to a pre-defined plane. It's utility is similar to other planar3D hydraulic fracture simulators (see review of Lecampion et al[55]), with the key novelty of enabling accurate solutions on very coarse meshes by embedding an appropriate tip asymptotic behavior and then computing the moving boundary condition of the advancing crack tip through an implicit time stepping method that projects the front location based on these known asymptotics. Like several other planar 3D hydraulic fracture simulators, the elasticity equation is solved using a 3D displacement discontinuity method and fluid flow is solved using the Finite Volume method. The following parameter set is used for both the C3Frac and ILSA II simulations:

$$E=9.5\ \text{GPa},\ \nu=0.2,\ K_{IC}=0\ \text{MPa}\cdot\text{m}^{1/2},$$

$$\mu=1\ \text{Pa}\cdot\text{s},\ Q_o=0.1\ \text{m}^3/\text{s},\ Z=20\ \text{m},$$

$$\sigma_o=70\ \text{Mpa},\ R_w=0.2\text{m}.$$

For each case, we present comparisons of the time evolution of fracture radius, fluid influx to each fracture, fracture opening at the center, and total fracture area. We also present three-dimensional plots showing the radius of each HF with color scale corresponding to the HF width. Figs. 3 and 4 show results from a case where the HFs are uniformly spaced so that h_1 = 5 m and hence fracture planes have z coordinates (in meters) z_1=0, z_2=5, z_3=10, z_4=15, and z_5=20. Figs. 5 and 6 show results corresponding to a non-uniformly spaced array in which fractures 2 and 4 are moved so that h_l=3.6 m, corresponding to fracture planes having z coordinates (in meters) z_1=0, z_2=3.6, z_3=10, z_4=16.4, and z_5=20. These results presented include: The dimensionless radius $R_i(t)/Z$, the inflow rate $q_i(R_w,t)$, the crack aperture at inlet $w_i(R_w,t)$ and total fracture area defined as

$$A(t)=\sum_{i=1}^{N-1} R_i^{\,2}(t)\,\pi \tag{34}$$

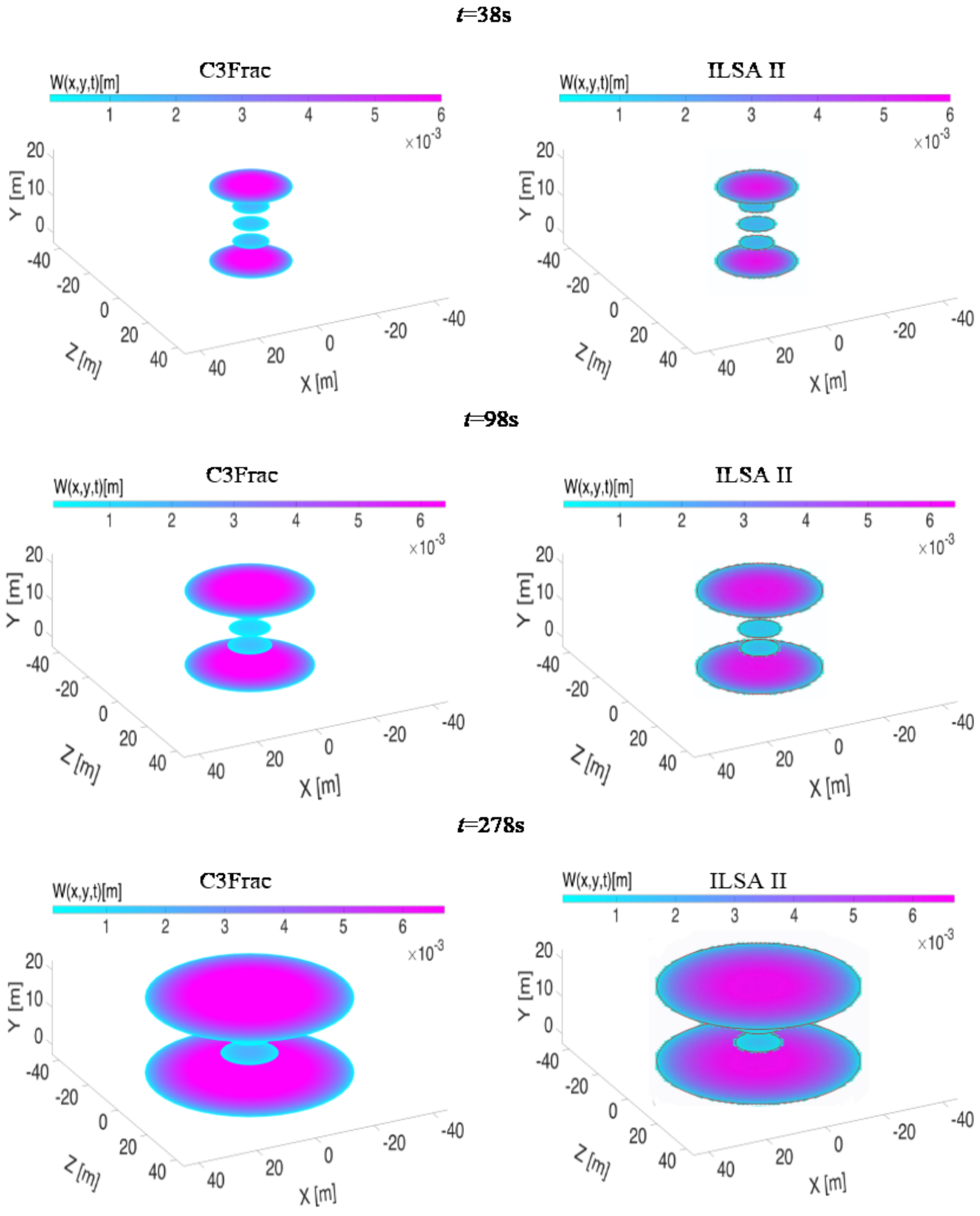

Fig. 3. Evolution for uniform spacing $h_1 = h_2 = h_3 = h_4$=5m, showing results from both C3Frac (ROM) and ILSA II (large scale).

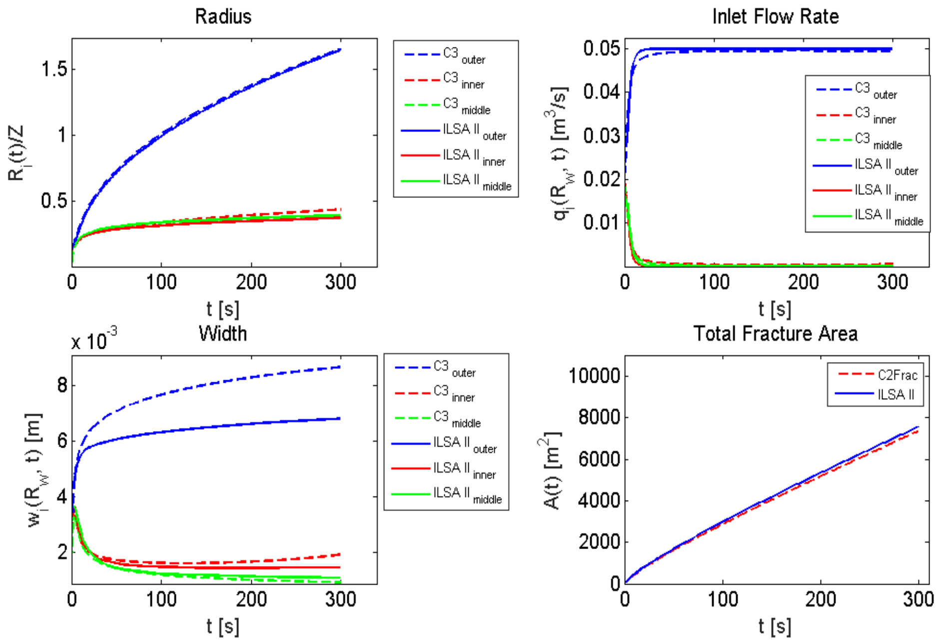

Fig. 4. C3Frac compared with ILSA II for a uniform array with $h_1 = h_2 = h_3 = h_4 = 5$m.

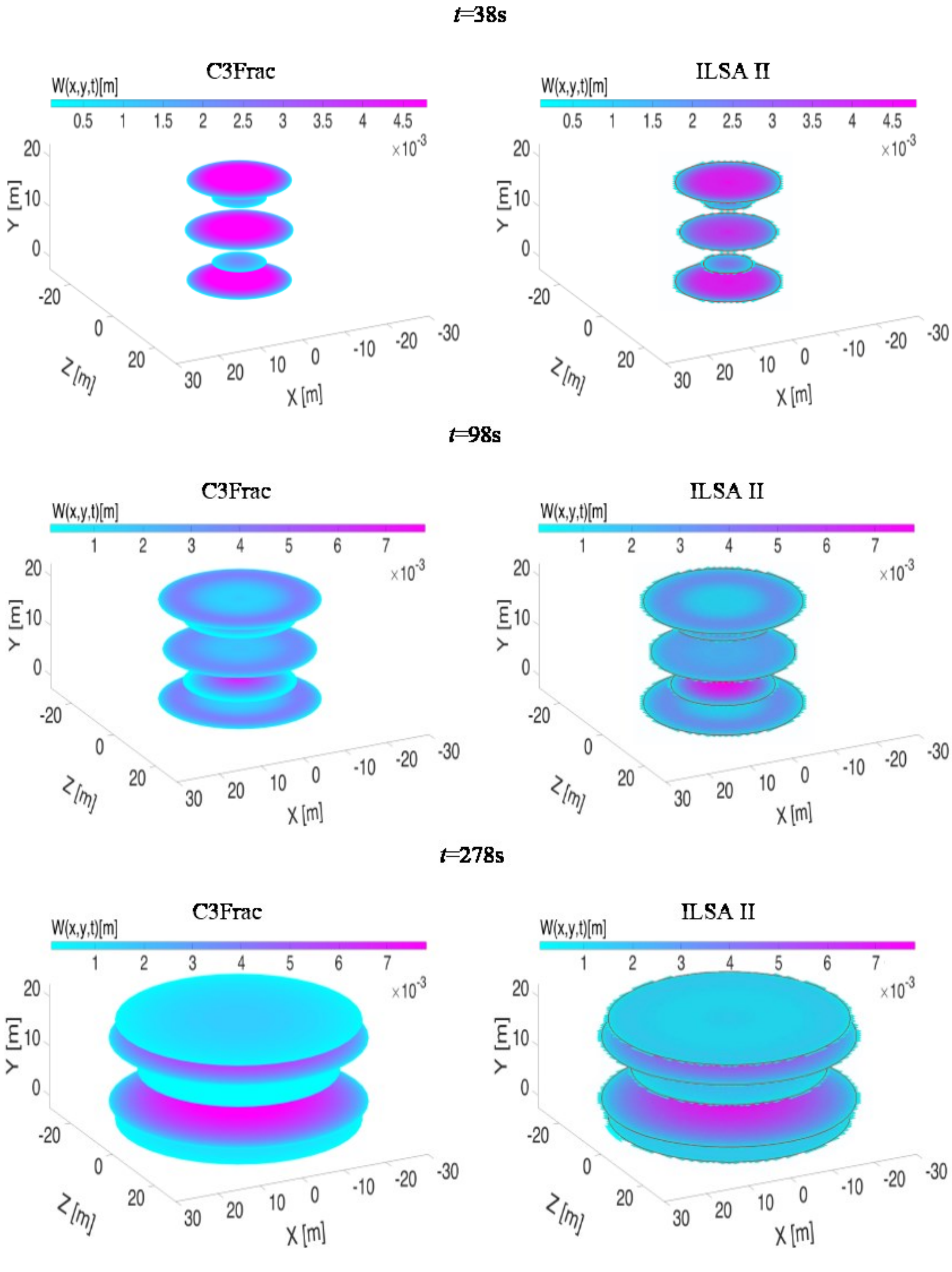

Fig. 5. Evolution for non-uniform spacing $h_1 = h_4 = 3.6$m and $h_2 = h_3 = 6.4$m.

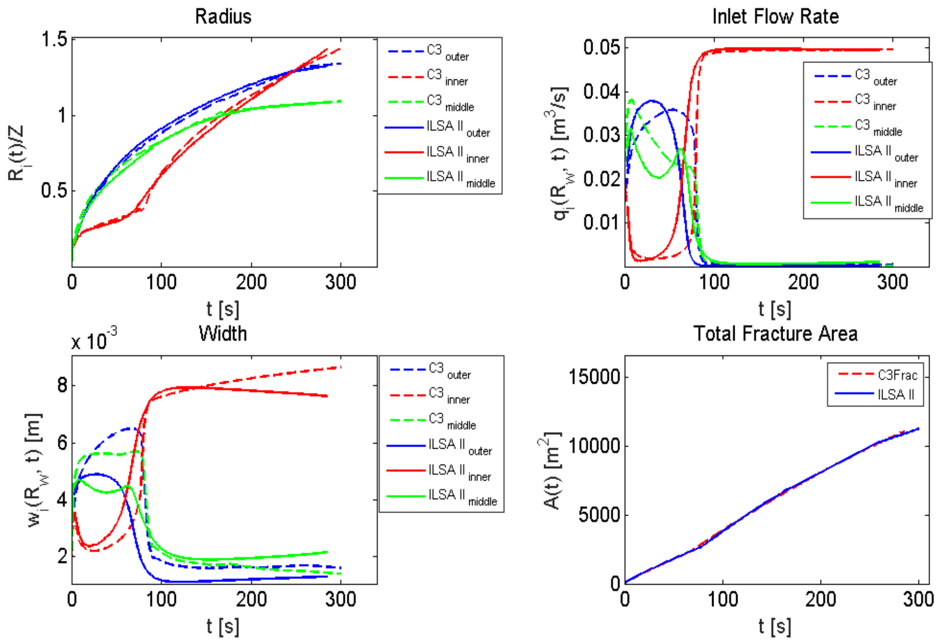

Fig. 6. C3Frac compared with ILSA II for non-uniform array with $h_1 = h_4$=3.6m and $h_2 = h_3$=6.4m.

Overall the ability of C3Frac to approximate the fracture radius and area is very good. The inlet flux is also adequately approximated, with several observations that can be made. Firstly, we observe the stress-shadowing phenomenon in which outer fractures grow preferentially while growth of the inner fractures is stunted. This phenomenon has also been observed by many others (e.g.[11-14]), and is strongly evidenced in the uniform spacing case (Fig. 4), where the inflow to the outer fracture increases sharply to 0.05m^3/s and consumes nearly all the total injection rate after 20 seconds. The localization of growth in the outer fractures is understandable because they have no constraint on their growth from outside the array. At the same time, flow rate to the other fractures decreases to approach zero. This is understood because the interior fractures have to compete with one another in an induced compressive stress field that is established by the outer fractures and enhanced by any additional growth by the interior fractures. The localization to the outer fractures becomes more pronounced with time while growth of the inner fractures is minimal for uniform spacing (h_I=5m) case (Fig. 3)

Upon changing the spacing h_I from 5m to 3.6m, the induced stresses from the inner fractures on the middle fracture decrease as the spacing between the inner and middle increases. Under this spacing, the inlet flow rate to the outer fractures consumes less of the total influx to the wellbore and the middle fracture's flow rate is only slightly less while the flow rate to the inner fracture remains almost constant with time. A similar behavior was observed by [19].

Further fracture growth is driven by a somewhat surprising mechanism. Capturing this mechanism is critical to matching the benchmark ILSA II simulations, and this was not possible with the prototype C2Frac model presented by [26]. The present work has focused on better approximating the stress interaction among the fractures especially when the radius exceeds the spacing. The "squeeze out" phenomenon (first observed by [19]) approximated by this new version C3Frac is described as follows. Due to the relative growth difference among the five fractures, the interaction stress induced from inner fractures obtains a negative value (tensile) near the tip. Combined with the impact of the moving boundary on the time derivative of the energy integral, a decreased interaction stress contribution is formed in the total energy balance for inner fractures via Eq. (28).

In the current example, the dominance of the fractures, 1, 3, and 5 is thus stopped by the reversal of the inner fractures at 50s (see Fig. 6). The fluid that was in these fractures in the region near the wellbore is subsequently displaced toward the perimeter as they are subjected to the induced stress associated with the now rapidly inflating inner fractures. This outward squeezing of the fluid has the effect of advancing the fracture by the displacing the fluid from the vicinity of the wellbore rather than by influx from the wellbore. A new phase is reached in which the role of the inner fractures switches from being passive and accepting relatively little fluid to accepting the majority of the fluid and actively driving the dynamics of the fracture development throughout the array. The increased uptake of fluid in the inner fractures also has a suppressing effect on outer fractures. As a side effect, the middle fracture gets a chance to take in more fluid from the wellbore, which is also depicted by a small rise (Fig. 6) shortly after t_s. At t=80s, the suppression effect from inner fractures also starts to affect middle fracture, and ultimately chokes further uptake of fluid into fractures 1, 3, and 5. Note that for the uniform spacing, the inner fractures never switch from being stunted to being dominant because they do not grow sufficiently to be impacted by the negative stress induced by the ratio *h/R*.

Besides the very good agreement between C3Frac and ILSA II, the C3Frac results also indicate the temporal and spatial character of crack opening (Fig. 6 and Fig. 4) in which the penny-shaped geometry is valid until the extension of the fracture becomes of the order of the stage length. As time goes on, a compressed region, approaching closure ($w_i(\rho_i, t) \cong 0$), appears owing to the interaction stress performed by inner fractures during the reversal process (Fig. 6).

Since the total fractured area can be related to the potential recovery of hydrocarbons (e.g.[4]), total fractured area is an important metric of hydraulic fracturing effectiveness (e.g.[19]). Here we define $A_{total}(t)$, which is the summation of surface area $A_i(t)$ over all the fractures, where $A_i(t) = \pi R_i(t)^2$. When all the fractures are small, so that their mutual stress interactions are insignificant, all configurations generate surface area at roughly the same rate and almost linearly with the time. However, for $t > 50$ s, because of the ever-increasing interaction effects, the h_1=3.6m case (12,000 m^2, Fig. 6) generates more area than the uniform cases (7,500 m^2, Fig. 4). Note that the same total volume is injected over the same time of pumping for these two cases. The reason for larger surface area in the non-uniform spacing case is a beneficial effect of the reversal fractures, causing dominance of fractures 2 and 4 in the latter part of the injection and an overall more uniform distribution of total volume among the 5 fractures. Hence these results show the total fractured area can be increased by more than 60% by selecting configurations for which h_1=3.6 m, as result consistent with [19].

Furthermore, non-uniform four and six fractures are also employed to test the validation between C3Frac and ILSA II. Fig. 7 shows results from a four fracture case where the HFs are non-uniformly spaced so that h_1 = 5 m and hence fracture planes have z coordinates (in meters) z_1=0, z_2=5, z_3=15, and z_5=20. Fig. 8 shows results for a non-uniformly spaced six-fracture array in which fractures 2, 3, 4 and 5 are moved so that h_1=2.75 m, h_2=4.25 m, corresponding to fracture planes having z coordinates (in meters) z_1=0, z_2=2.75, z_3=7, z_4=13, z_5=17.25 and z_5=20. The level of agreement between the ROM of C3Frac and the large scale model of ILSA II is similar to what was obtained for five fracture cases. We also note that the aforementioned “squeeze-out” is observed in the six fracture case but not in the four fracture case presented here, although further numerical experimentation may lead to discovery of squeeze-out in certain non-uniform four fracture cases as well.

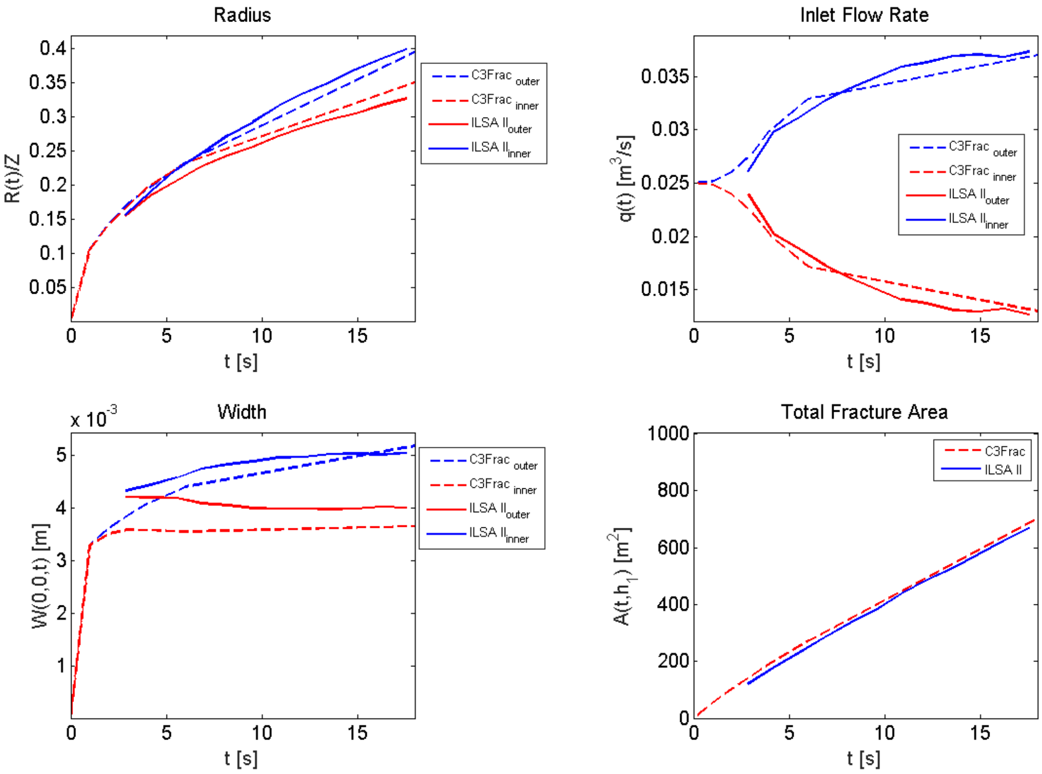

Fig. 7. C3Frac compared with ILSA II for a non-uniform four fracture array with h_1= h_3=4m, h_2=12m.

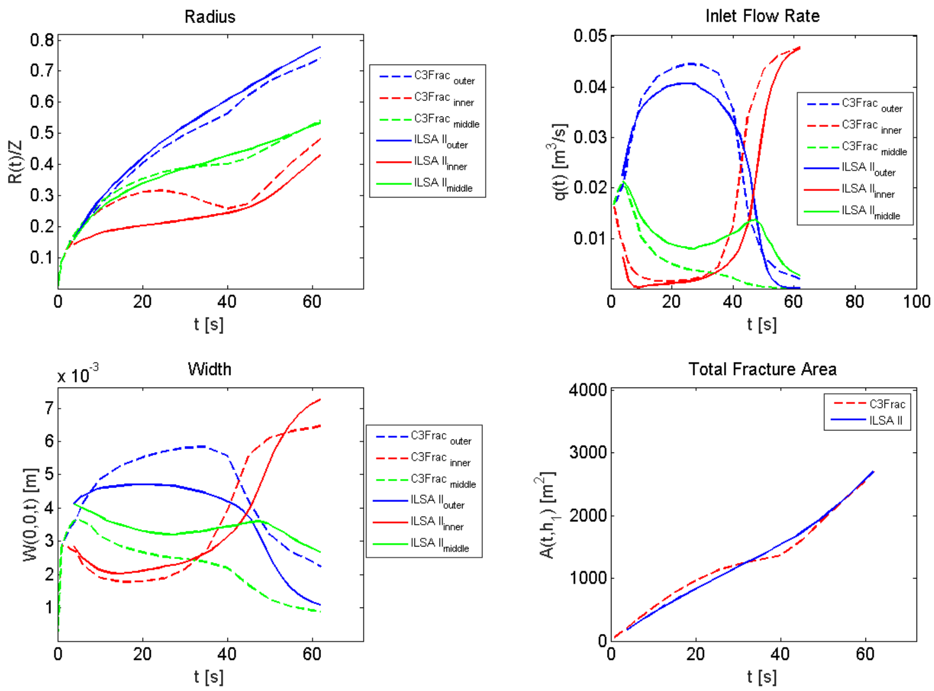

Fig. 8. C3Frac compared with ILSA II for non-uniform six fracture array with h_1= h_5=2.75m, h_2= h_4=4.25m and h_3=6m.

So far we have discussed the overall behavior of the system illustrated both by C3Frac and the ILSA II benchmarks. But most importantly, Figs. 3-8 show the similarity between C3Frac and ILSA II. Typically, C3Frac remains within 2% relative to the ILSA II benchmark for fracture area. The worst match is in the fracture opening at the wellbore, which is in about 10% discrepancy for the inner fracture and as much as 50% for the outer and middle fractures. Note that in the far field (short HF) previous version C2Frac [26], simulates the radial growth only in the range that R_{max}/Z is smaller than 0.6. Through the substantially modified solution method algorithm, the approximation to the benchmark ILSA II is achieved even after the fracture radii exceed the total stage length.

Table 1

Computation time compare between C2Frac, C3Frac and ILSA II for uniform fracture array at same simulation time and steps.

Uniform Five	C2Frac	C3Frac	ILSA II
Computation time	1.06s	255 s	220612 s
Simulation time & Steps	t=203 s 128 steps	t=203 s 128 steps	t=203 s 128 steps
Processer & RAM	INTEL-i7 4770k 4.00 GHz. 32 GB RAM	INTEL-i7 4770k 4.00 GHz. 32 GB RAM	INTEL-XEON E5649 2.53 GHz 96 GB RAM

While achieving the previously-demonstrated accuracy, the simulator takes only minutes to compute a single multi-fracture result at typical reservoir length and time scales on a personal computer. Although this is much slower than C2Frac, which computes in a few seconds, the benefit is the ability to simulate even when the fractures are long relative to their separation. To this point, an illustration of computation time for C2Frac, C3Frac, and ILSA II is presented in Table 1. Note, however, that the computation time of ILSA II for each time step continuously increases because the advancing front leads to an ever-increasing number of elements in the simulation, there is no such increase in computation time per model time step in C2Frac or C3Frac. We also note that there is a possibility to significantly speed up the simulations by combining C2Frac and C3Frac, where the former is used to simulate growth until the maximum fracture length reaches some threshold (say, around half of the stage length), after which C3Frac is used to compute the rest of the growth, For example, in h_I=3.6m case, before the squeeze out effect occurs (the point in time where the C3Frac enhancement become most important), the fracture growth can be well-approximated by C2Frac in seconds, which in this case would save 3 minutes of computation time over using C3Frac only. Either way, the simulations are much faster than fully coupled simulations, which can take tens of hours and up to a week to compute on a similar computer. Because of the speed of calculation and reasonable accuracy, this new approximate simulator opens new possibilities to explore large parametric spaces, identifying combinations of parameters associated with optimal behaviors (i.e. maximizing fracture surface area) and enabling time consuming but accurate fully-coupled simulations to be focused on these regions of interest in the parametric space that governs the behavior of the system.

5 Parametric Study

A few examples illustrate the optimization enabled by the rapid computation times associated with C3Frac. The metric by which we evaluate the performance of a given configuration is taken as the total surface area of all the fractures in the array until time t, which we represent by $A(t;\, h_I)$. It is useful to normalize by $A^*(T)$, the total fracture area of N non-interacting fractures each taking the same total volume of fluid and growing exactly uniformly according to the relevant analytical solution [27]. The ratio $A(t;\, h_I)/\, A^*(T)$ represents the relative change in the total fractured area that is achieved by adjusting h_I. We plot $A(T;\ h_I)/\ A^*(T)$ as a function of the dimensionless configuration parameter $h_I(N\text{-}1)/Z$, with various stage lengths Z and injection rates Q. These results are presented in Figs. 7 and 8, where we note that the uniform spacing $h_I = Z/(N\text{-}1)$ is represented as 1, while its limiting values of 0 and 2 correspond to non-uniform limiting cases with h_I=0 (touching of fractures 1-2 and 4-5) and h_I= 2*$Z/(N\text{-}1)$ (touching of fractures 2-3-4), respectively.

First, we illustrate the impact of stage length, keeping all other quantities such as injection rate and time equal, Fig. 7. We compare results for stage length Z = 25m, 50m and 100m. We observe that the uniformly-spaced configuration, coming with a significant stress shadow especially at Z=50 and 100m, corresponds to a lower normalized area around 0.75. By decreasing h_I below $Z/(N\text{-}1)$, that is, by moving the 2nd and 4th fractures away from the center fracture as suggested by [19], results in 80% to 120% relative increase in the total fractured area. This increase comes for all stage lengths, despite the existence of some important differences. Most notably, a smaller interval ratio $h_I(N\text{-}1)/Z$ is required to maximize the generated area for the largest stage length. This is because such a small interval length is needed to stimulate the squeezing effect, which turns out to have an important impact on maximizing the fracture area. Also note that the sensitivity of the total, final area to the spacing (derivative of the plots in Fig. 7) tends to be greater for the larger interval length and at larger injection times, meaning that such spacing optimization is more important when interval lengths and/or injection times are large.

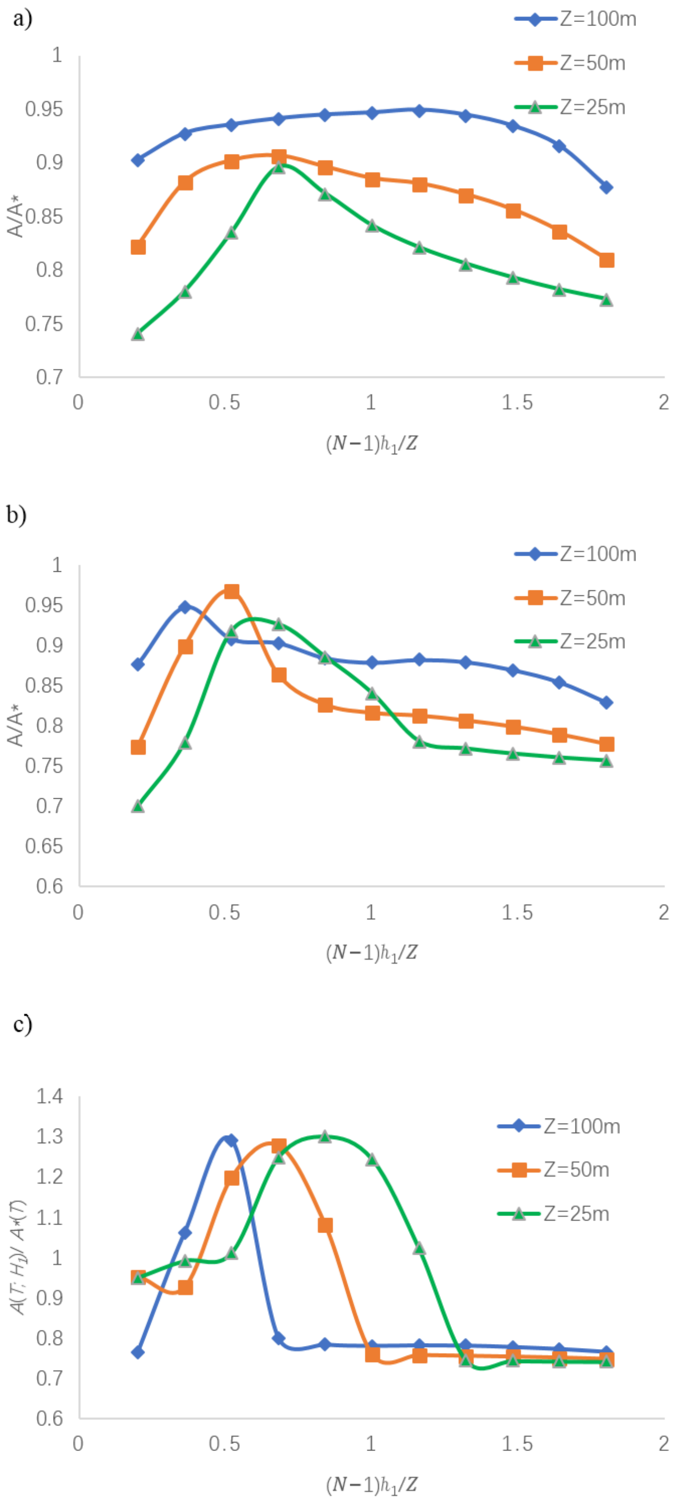

Fig. 7. Normalized dimensionless total fracture area $A(T;\, h_1)/\, A^*(T)$ evolution with various stage length Z in the five-fracture array for different values of the spacing h_1 for Q=0.2 m^3/s and t as a) 50 s b) 300 s c)3600 s.

The prior increases in productivity (inferred from the surface area) of uniform spacing stimulations by using smaller stage lengths Fig. 7 come without need for increasing injection rate. To investigate if there is benefit in optimizing in terms of injection rate, we plot the normalized area $A(T;\ h_I)/\ A^*(T)$ versus the configuration perturbation parameter h_I for a representative selection of values of the injection rate Q_o given by 0.1m^3/s, 0.2m^3/s and 0.3m^3/s, adjusting injected volume to ensure satisfaction of the viscosity regime requirement. The total injection volume is preset as 120 m^3 and 720 m^3 and stage length is 50m.

We observe that the shapes of these curves are very similar, but a little shifted over the range of values of the configuration parameter considered. This is due to fluid flow that follows Poiseuille law, Eq. (4). For the sake of argument, assume we can ignore differences in the pressure gradient between fracture entry points. Then the crack opening near the inlet $w_i(R_w, t)$ is proportional to the inlet flow rate $q_i(t)^{1/3}$. When the injection rate is set to be 0.2 m^3/s, the crack width is 1.26 times larger than in the case where Q_o=0.1 m^3/s. Hence, for the same injected volume, the cases with larger average width (opening) give a smaller fracture area. This relationship is the cause of the observed differences in Fig. 8, where Q_o =0.1 m^3/s leads to about 30% more fractured area than Q_o =0.2 m^3/s. Otherwise, for a given injection rate, the total crack opening is maximized for the spacing that also achieves the maximum area, as illustrated by Fig. 8(a) and Fig. 8(b). The reason is that flow rate becomes the most uniform in its distribution at that spacing. This observation holds for a while, until the fractures become very long relative to their spacing. In this super-near-field region, the fracture opening profile indicates that the opening in the vicinity of the tip increases at the cost of decreasing the opening of the central portion Fig. 5. Thus, the maximum width eventually does not correspond to the spacing that generates the maximum area.

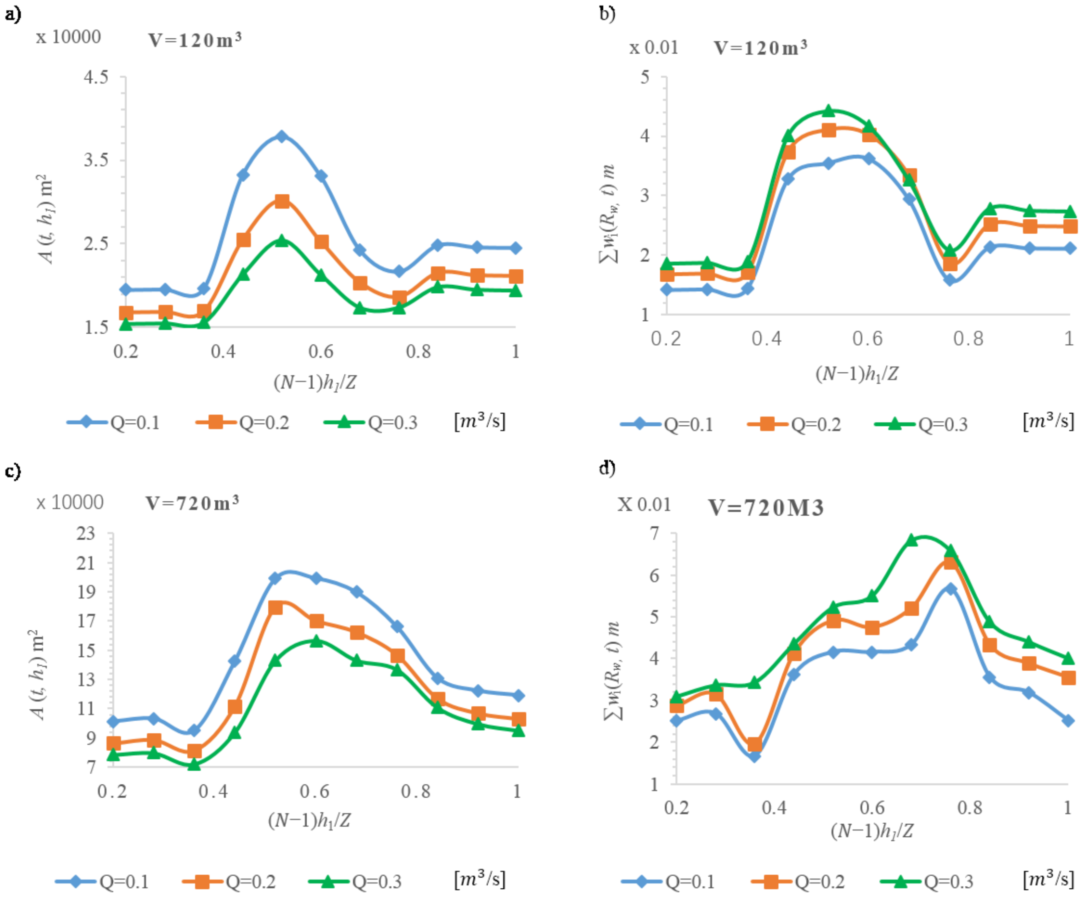

Fig. 8. Illustrative examples of injection rate effect for total fractured area $A(T, h_1)$ and summation of near wellbore width $\sum W(0,T, h_1)$ respectively, in which the HF parameters such as input volume are set as a)120 m^3 b) 120 m^3 c)720 m^3 d) 720 m^3

6 Conclusion

A new approximate ROM simulator, C3Frac, rapidly predicts how mechanical interaction among simultaneously growing radial hydraulic fractures effects their growth. This approximate simulation method is based on preserving global volume and energy balance and the elastically-determined crack opening while approximating the fluid flow via a functional form preserving the pressure gradient near the inlet and tip and approximating the interaction stresses based on the analytical solution for uniformly pressurized cracks with the same length and volume as each hydraulic fracture. Validating through comparison to results from a fully-coupled, large scale planar 3D model (ILSA II) confirm the accuracy of the approximation, especially for prediction of the length of each fracture and the overall created fracture surface area.

The ROM is able to capture complex coupled phenomena. When the spacing between fractures is uniform, the model confirms the phenomenon of stress shadowing in which growth of one or more fractures is suppressed by the stresses generated by their neighbors. However, we have also shown that the model captures a "squeeze out" phenomenon that takes place for certain non-uniform fracture spacing configurations when the fracture radii substantially exceed the spacing. Simulations suggest there is the potential to increase the total fractured area in the array after 3600 seconds of pumping by 100% compared to the uniform array for which the squeeze out effect does not occur and the inner fractures are simply suppressed in their growth.

The ROM simulator computes within a few minutes on a typical personal computer, thereby enabling wide ranging parametric studies and optimization that requires hundreds of model evaluations. As a demonstration of this capability, it is shown that non-uniform spacing is one of several ways to impact the uniformity and total surface area of created fractures. Stage length and injection rate also provide variable parameters for optimization. From our study, strategic stage length choice is shown to be a complimentary approach. Somewhat counter-intuitively, we show decreasing stage length can actually lead to improvement in the ability to generate fracture surface area with relatively uniform spacing because of the ability of shorter stage lengths to trigger the squeeze out effect. The numerical experiments also indicate that smaller injection rate generates more fracture area for a given injected volume, as expected due to the lower net pressure and resulting fracture opening. As a tradeoff, such a design will decrease the capacity for proppant admittance due to the smaller opening.

In summary, this work provides not only a new method for reduced order modeling of hydraulic fractures, but also, practically, a demonstration that the stress shadow effect can be modified and to some degree mitigated through selectable treating conditions such as fracture spacing, stage length, and injected volume. While beyond the present scope, there is more that can be optimized such as fluid flow rate, fluid viscosity, and so on. Future work will aim at expanding capability for optimizing horizontal well completions. These efforts will firstly be aimed at including the impact of leak off, fracture toughness, and the presence of height growth barriers. Future work will also focus on including proppant transport and developing benchmark laboratory and field experiments.

Acknowledgements

This material is based upon work supported by the University of Pittsburgh Center for Energy, Swanson School of Engineering, Department of Chemical and Petroleum Engineering, and Department of Civil and Environmental Engineering. Additional support for recent advances to this work was provided by the National Science

Foundation under Grant No. 1645246.

References

[1] R.G. Jeffrey, A.P. Bunger, B. Lecampion, X. Zhang, Z. Chen, A. van As, D. P. Allison, W. De Beer, J. W. Dudley, E. Siebrits, M. Thiercelin, M. Mainguy, Measuring Hydraulic Fracture Growth in Naturally Fractured Rock, in: Proceedings SPE Annual Technology Conference and Exhibition, New Orleans, Louisiana, USA, 2009.

[2] A.S. Abou-Sayed, Q. Guo, F. Meng, K. Zaki, (2003, January 1). Ultimate Capacity of a Disposal Well in Drilling Waste Injection Operations, in: Proceedings SPE/IADC Drilling Conference, Amsterdam, Netherlands, 2003.

[3] L.K. Regenauer, A.P. Bunger, H.T. Chua, A. Dyskin, F. Fusseis, O. Gaede, R.G. Jeffrey, A. Karrech, T. Kohl, J. Liu, V. Lyakhovsky, E. Pasternak, R. Podgorney, S. Rahman, C. Schrank, M. Trefry, M. Veveakis, B. Wu, D. Yuen, F. Wellmann, X. Zhang, Deep Geothermal: The ‘Moon Landing’ Mission in the Unconventional Energy and Minerals Space, J. Earth Sci., 26 (2015) 2-10.

[4] M. Economides, K. G. Nolte, Reservoir Stimulation, John Wiley & Sons, 2000.

[5] T.M. Carl, B.S. Michael, Hydraulic Fracturing: History of an Enduring Technology, J. Petrol. Tech. 62 (2010) 26-40.

[6] B. Lecampion, J, Desroches. Simultaneous initiation and growth of multiple radial HFs from a horizontal wellbore, J. Mech. Phys. Sol. 82 (2015) 235–258.

[7] C. Miller, G. Waters, E. Rylander, Evaluation of production log data from

horizontal wells drilled in organic shales. in: Proceedings SPE North American Unconventional Gas Conference and Exhibition, The Woodlands, Texas, USA, 2011, SPE 144326.

[8] J.D. Baihly, R. Malpani, C. Edwards, S.Y. Han, J.C.L. Kok, E.M. Tollefsen, C.W. Wheeler, Unlocking the shale mystery: How lateral measurements and well placement impact completions and resultant production, in: Proceedings SPE Tight Gas Completions Conference. San Antonio, Texas, USA, 2010, SPE 138427.

[9] C. Cipolla, X. Weng, H. Onda, T. Nadaraja, U. Ganguly, R. Malpani, New algorithms and integrated workflow for tight gas and shale completions, in: Proceedings SPE Annual Technology Conference and Exhibition. Denver, Colorado, USA, 2011, SPE 146872.

[10] A.P, Bunger, D.J. Cardella, Spatial distribution of production in a Marcellus Shale well: Evidence for hydraulic fracture stress interaction, J. Pet. Sci. Eng. 113 (2015) 162-166.

[11] M.K. Fisher, J.R. Heinze, C.D. Harris, B.M. Davidson, C.A. Wright, K.P. Dunn, Optimizing horizontal completion techniques in the Barnett shale using microseismic fracture mapping. In Proceedings SPE Annual Technology Conference and Exhibition. Houston, Texas, USA, 2004, SPE 90051.

[12] H.H. Abass, M.Y. Soliman, A.M. Tahini, J. Surjaatmadja, D.L. Meadows, L. Sierra L, Oriented fracturing: A new technique to hydraulically fracture an openhole horizontal well, in: Proceedings SPE Annual Technical Conference

and Exhibition. New Orleans, LA, USA, 2009, SPE 124483.

[13] B. Meyer, L. Bazan, A discrete fracture network model for hydraulically induced fractures-theory, parametric and case studies, in: Proceedigs SPE Hydraulic Fracturing Technology Conference and Exhibition. The Woodlands, Texas, USA, 2011, SPE 140514.

[14] L.N. Germanovich, L.M. Ring, D.K. Astakhov, J. Shlyapobersky, M.J. Mayerhofer, Hydraulic fracture with multiple segments - I: Observations and model formulation, Int. J. Rock Mech. Min. Sci., 34 (1997) 98e1-98e15

[15] J.E. Olson, Multi-fracture Propagation Modeling: Applications to Hydraulic Fracturing in Shales and Tight Gas Sands, in: Proceedings of 42nd US Rock Mechanics Symposium, San Francisco, California, 2008, pp. 08-327.

[16] O. Kresse, X. Weng, H. Gu, et al. Numerical Modeling of Hydraulic Fractures Interaction in Complex Naturally Fractured Formations, Rock. Mech. Rock. Eng. 46 (2013) 555-568.

[17] K. Wu, J.E. Olson, Investigation of critical in situ and injection factors in multifrac treatments: Guidelines for controlling fracture complexity, in: Proceeding SPE Hydraulic Fracturing Technology Conference, The Woodlands, Texas, 2013, SPE 163821.

[18] B. Lecampion, J. Desroches, X. Weng, J. Burghardt, J.E. Brown, Can We Engineer Better Multistage Horizontal Completions? Evidence of the Importance of Near-Wellbore Fracture Geometry From Theory, Lab and Field Experiments, in: Proceeding SPE Hydraulic Fracturing Technology Conference, The

Woodlands, Texas, USA, 2015, SPE 173363.

[19] A.P. Peirce, A.P. Bunger, Interference Fracturing: Non-Uniform Distributions of Perforation Clusters that Promote Simultaneous Growth of Multiple HFs, SPE. J. 20 (2015) 384-395.

[20] M. Izadi, S. Dubljevic, Order-reduction of parabolic PDEs with time‐varying domain using empirical eigenfunctions, AICHE. J. 59 (2013) 4142-4150.

[21] M. Izadi, S. Dubljevic, Computation of empirical eigenfunctions of parabolic PDEs with non-trivial time-varying domain, in: Control Conference (ECC), European, 2013, 53-58.

[22] H.S. Sidhu, A. Narasingam, P. Siddhamshetty, J.S.I. Kwon, Model order reduction of nonlinear parabolic PDE systems with moving boundaries using sparse proper orthogonal decomposition: Application to hydraulic fracturing, Comput. Chem. Eng. 112 (2018) 92-100.

[23] A. Narasingam, J.S.I. Kwon, Development of local dynamic mode decomposition with control: Application to model predictive control of hydraulic fracturing, Comput. Chem. Eng. 106 (2017) 501-511.

[24] A. Narasingam, P. Siddhamshetty, J.S.I. Kwon, Temporal clustering for order reduction of nonlinear parabolic PDE systems with time‐dependent spatial domains: Application to a hydraulic fracturing process, AICHE. J. 63 (2017) 3818-3831.

[25] A.P. Peirce, E. Detournay, An implicit level set method for modeling hydraulically driven fractures. Computer Meth. Appl. Mech. Eng. 197 (2008)

2858–2885.

[26] C. Cheng, A.P. Bunger, Rapid Simulation of Multiple Radially-Growing HFs Using an Energy-Based Approach. Int. J. Numer. Anal. Meth. Geomech. 40 (2016)1007-1022.

[27] A.A, Savitski, E. Detournay, Propagation of a penny-shaped fluid-driven fracture in an impermeable rock: asymptotic solutions. Int. J. Solids Struct. 39 (2002) 6311–6337.

[28] A.P. Bunger, R.G. Jeffrey, X, Zhang, Constraints on Simultaneous Growth of HFs from Multiple Perforation Clusters in Horizontal Wells, SPE. J. 19 (2014) 608-620.

[29] N.P. Roussel, R. Manchanda, M.M. Sharma, Implications of Fracturing Pressure Data Recorded during a Horizontal Completion on Stage Spacing Design, in: Proceeding SPE Hydraulic Fracturing Technology Conference, The Woodlands, Texas, USA, 2012, SPE 152631.

[30] V. Sesetty, A. Ghassemi, Numerical simulation of sequential and simultaneous hydraulic fracturing, in: A. P. Bunger, J. McLennan, R. G. Jeffrey (Eds.), Effective and Sustainable Hydraulic Fracturing, Intech, Rijeka, Croatia, 2013, (Chapter 33).

[31] A.P. Bunger, X. Zhang, R.G. Jeffrey, Parameters effecting the interaction among closely spaced HFs. SPE. J. 17 (2012) 292–306.

[32] J. R. Rice, Mathematical Analysis in the Mechanics of Fracture, Academic Press, New York, 1968, pp. 191-311

[33] G.R. Irwin, Analysis of stresses and strains near the end of a crack traversing a plate, ASME J. Appl. Mech. 24 (1957) 361–364.

[34] M.F. Kanninen, C.H. Popelar,. Advanced Fracture Mechanics, In: volume 15 of The Oxford Engineering Science Series, Oxford University Press, Oxford, UK,1985.

[35] G.K. Batchelor, Brownian diffusion of particles with hydrodynamic interaction, J. Fluid Mech. 74 (1976) 1–29.

[36] D. Garagash, Hydraulic fracture propagation in elastic rock with large toughness. In: Girard J. Liebman M. Breeds C. Doe T. (Eds.), Rock Around the Rim—Proceedings of the Fourth North American Rock Mechanics Symposium. Balkema, Rotterdam, (2000) 221–228.

[37] J. Olson, D.D. Pollard, Inferring paleostresses from natural fracture patterns: A new method: Geology, 17 (1989) 345-348.

[38] X. Weng, Fracture Initiation and Propagation From Deviated Wellbores, in: Proceeding SPE Annual Technical Conference and Exhibition, Houston, Texas, United States, 1993, SPE 26597.

[39] J.E. Olson, Fracturing from Highly Deviated and Horizontal Wells: Numerical Analysis of Non-planar Fracture Propagation, in: Proceedings Low Permeability Reservoirs Symposium, Denver, Colorado, 1995, SPE 29573.

[40] J.E. Olson, A. Dahi-Taleghani, Modeling simultaneous growth of multiple hydraulic fractures and their interaction with natural fractures, in: Proceeding Society of Petroleum Engineers - SPE Hydraulic Fracturing

Technology Conference, The Woodlands, Texas, United States, 2009, SPE 119739.

[41] T.K. Perkins, L.R. Kern, Widths of HFs. J. Pet. Tech. 13 (1961) 937–949.

[42] R.P. Nordgren, Propagation of a Vertical HF, SPE. J. 12 (1972) 306–314.

[43] C. Cheng, A.P. Bunger, A.P. Peirce. Optimal Perforation Location and Limited Entry Design for Promoting Simultaneous Growth of Multiple Hydraulic Fractures, in: Proceedings SPE Hydraulic Fracturing Technology Conference, The Woodlands, Texas, United States, 9-11 February 2016. SPE 179158.

[44] B. Lecampion, J. Desroches, Simultaneous initiation and growth of multiple radial hydraulic fractures from a horizontal wellbore, J. Mech. Phys. Solids. 82 (2015) 235-258.

[45] S.A. Khristianovich, Y.P. Zheltov, Formation of Vertical Fractures by Means of Highly Viscous Liquid, Proc., Fourth World Pet. Congress, Rome 2 (1955) 579–586.

[46] I.N. Sneddon, Fourier Transforms, McGraw-Hill, New York, 1951.

[47] G.K. Batchelor, An Introduction to Fluid Dynamics, Cambridge University Press, Cambridge UK, 1967.

[48] E. Detournay, Propagation regimes of fluid-driven fractures in impermeable rocks. Int. J. Geomech. 4 (2004) 1–11.

[49] E. Detournay, A, Peirce, On the moving boundary conditions for a hydraulic fracture, Int. J. Eng. Sci. 84 (2014) 147–155.

[50] I.N. Sneddon, The distribution of stress in the neighborhood of a crack in an elastic solid, Proc. Roy. Soc. London A, 187 (1946) 229-260,

[51] D.A. Spence, P.W. Sharp, Self-similar solutions for elastohydrodynamic cavity flow, Proc. Roy. Soc. London, Ser. A, 400 (1985) 289-313.

[52] D.D. Garagash, E. Detournay, The Tip Region of a Fluid-Driven Fracture in an elastic medium. ASME. J. Appl. Mech. 67(1999):183-192.

[53] A.P. Bunger, Analysis of the power input needed to propagate multiple HFs, Int. J. Solids. Struct. 50 (2013) 1538–1549.

[54] B. Lecampion, E. Detournay, An implicit algorithm for the propagation of a plane strain hydraulic fracture with fluid lag, Comput. Meth. Appl. Mech. Eng. 196 (2007) 4863–4880.

[55] B. Lecampion, A.P. Bunger, X. Zhang, Numerical Methods for Hydraulic Fracture Propagation: A Review of Recent Trends. J. Nat. Gas. Sci. Eng. 49 (2018) 66-83.